NUCLEAR DOMINATED ACCRETION FLOWS IN TWO DIMENSIONS. I. TORUS EVOLUTION WITH PARAMETRIC MICROPHYSICS

RODRIGO FERNÁNDEZ[1,2] AND BRIAN D. METZGER[2,3]
Draft version September 14, 2012

ABSTRACT

We explore the evolution of radiatively inefficient accretion disks in which nuclear reactions are dynamically important ('Nuclear Dominated Accretion Flows', or NuDAFs). Examples of such disks are those generated by the merger of a white dwarf with a neutron star or black hole, or by the collapse of a rotating star. Here we present two-dimensional hydrodynamic simulations that systematically explore the effect of adding a single nuclear reaction to a viscous torus. The equation of state, anomalous shear stress, and nuclear reactions are given parametric forms. Our results point to the existence of two qualitatively different regimes of NuDAF evolution: (1) steady accretion with quiescent burning; or (2) detonation of the disk. These outcomes are controlled primarily by the ratio Ψ of the nuclear energy released to the enthalpy at the burning radius. Disks detonate if Ψ exceeds a critical value $\Psi_{\rm crit} \sim 1$, and if burning occurs in regions where neutrino cooling is unimportant. Thermonuclear runaways are seeded by the turbulent mixing of hot ash with cold fuel at the burning front. Disks with $\Psi < \Psi_{\rm crit}$ do not explode, but instead power a persistent collimated outflow of unbound material composed primarily of ash, with a mass-loss rate that increases with Ψ. We discuss the implications of our results for supernova-like counterparts from astrophysical events in the NuDAF regime. In particular, detonations following a white dwarf - neutron star merger could account for some subluminous Type Ia supernovae, such as the class defined by SN 2002cx.

Subject headings: accretion, accretion disks — nuclear reactions, nucleosynthesis, abundances — white dwarfs — hydrodynamics — stars: winds, outflows — supernovae: general

1. INTRODUCTION

Many violent and visually spectacular astrophysical events involve stellar material collapsing at high rates onto a central compact object. Examples include the core collapse of a massive star to form a neutron star (NS) or black hole (BH) remnant (Woosley et al. 2002); the accretion-induced collapse of a white dwarf (WD) (Nomoto & Kondo 1991); the merger of binary compact objects, including various combinations of WDs, NSs, and BHs; the binary merger of a Helium star with a NS or BH (e.g., Fryer & Woosley 1998); and the inspiral and tidal disruption of a planet that is engulfed by the envelope of its host star (e.g., Siess & Livio 1999). Although only some of these events have yet been unambiguously observed, this situation may change soon as the result of new transient surveys coming online across the electromagnetic spectrum.

In many of the above examples, angular momentum places a key dynamical role, such that a significant fraction of the infalling matter forms a rotationally-supported torus around the central object. If the accretion rate through such a disk is sufficiently high, then the heat generated is trapped in the flow instead of being efficiently radiated away (e.g., Chevalier 1993). Such disks are examples of what is generally termed a *Radiatively Inefficient Accretion Flow* (RIAF).[4]

Previous theoretical work on RIAFs has focused on understanding their spatial structure and on determining the processes that control the radial transport of mass, energy, and angular momentum through the disk. The ADAF model (Narayan & Yi 1994, 1995) assumes that angular momentum is transported outward by turbulent stresses (mediated by, e.g., the magnetorotational instability [MRI]; Balbus & Hawley 1998) and that thermal energy is advected through the inner boundary of the disk at small radii. The CDAF model (Quataert & Gruzinov 2000) postulates that outward angular momentum transport is offset by *inward* transport by convection. The resulting accretion rate is much lower than that arising from ADAFs, though all of the disk material is eventually accreted by the central object. In contrast, the ADIOS model (Blandford & Begelman 1999) assumes that most of the accretion energy powers an unbound outflow from the disk, such that the majority of the material never reaches the central object.

Numerous two- and three dimensional global simulations of RIAFs have been performed in hydrodynamics (2D - Stone et al. 1999, Igumenshchev & Abramowicz 2000; 3D - Igumenshchev et al. 2000) as well as in magnetohydrodynamics [MHD] (2D - Stone & Pringle 2001; 3D - Hawley et al. 2001, Machida et al. 2001, Hawley & Balbus 2002, Igumenshchev et al. 2003, Pen et al. 2003, Pang et al. 2011, McKinney et al. 2012, Narayan et al. 2012). A key conclusion of most such simulations to date is that the net accretion rate through the inner edge of the torus at $r = r_{\rm in}$ is substantially reduced (by a factor $\sim r_{\rm in}/R_0$) from the feeding rate set by the outer torus at $r = R_0$, consistent with both CDAF and ADIOS models (e.g., Yuan et al. 2012). However, the relative importance of truly unbound outflows versus simply large-scale bound convective motions remains under debate (e.g., Abramowicz et al. 2000).

Here we focus on another key feature of RIAFs in collapsar and merging compact object scenarios: the nuclear composition of the accreting material and its effect on the dynamics of the accretion disk. If the potential well of the primary has

---

[1] Institute for Advanced Study. Einstein Drive, Princeton, NJ 08540, USA.
[2] Einstein Fellow
[3] Department of Astrophysical Sciences, Peyton Hall, Princeton University, Princeton, NJ 08544, USA.
[4] The high density RIAFs discussed here are to be distinguished from those that occur at much lower densities due to inefficient two-body collisional cooling, and which are used to model low-luminosity AGN.

an appropriate depth, then the inflowing matter becomes sufficiently hot and dense for nuclear reactions to become dynamically important and to generate radioactive material. Depending on how nuclear burning affects the accretion rate onto the central object, or the properties of outflows from the disk, this can greatly impact predictions for the observational signatures of these events.

Metzger (2012; hereafter M12) constructed a steady-state, height-integrated model of accretion following the tidal disruption of a WD by a BH or NS, including the effects of nuclear burning on both the thermodynamics and composition of the accreting material. He adopted an ADIOS-type model, in which the properties of the outflow from each radius in the disk are calculated by locally balancing wind cooling with viscous and nuclear heating. In this model, the additional heating from nuclear burning acts to enhance the mass loss rate in the outflow over its nominal value without nuclear burning. M12 showed that at radii $r \lesssim 10^9$ cm, the midplane density and temperature become sufficiently high to burn the initial white dwarf material into increasingly heavier elements (e.g., Mg, Si, S, Ca, Fe, and Ni) at sequentially smaller radii. The disk structure thus resembles the onion-like structure of a massive star, but one which evolves on a much more rapid timescale. The combined outflow from all annuli in the disk is composed primarily of unburnt WD material from the outer disk, along with a smaller fraction of intermediate mass elements and radioactive ^{56}Ni originating from smaller radii.

In some regions of the disk M12 found that the energy released by nuclear reactions is at least comparable to that released viscously, thus motivating him to term this novel accretion regime a *Nuclear Dominated Accretion Flow* (NuDAF). Because RIAFs are already only marginally bound, even a modest additional source of energy can have a significant impact on its structure. In other words, the properties of NuDAFs could in principle differ markedly from the predictions of normal ADAF/CDAF/ADIOS models.

Given its many simplifying assumptions, the M12 model cannot address several key questions relevant to NuDAFs. These include (1) the true effects of nuclear burning on the quantity and composition of disk outflows; (2) multi-dimensional effects, such as radial convective mixing or the diffusion of burnt fuel upstream; (3) the long-term, global evolution of the disk; and (4) the thermal stability of the inflow, which is subtle due to the sensitive temperature dependence of the nuclear reaction rates. M12 found that thermal stability depends critically on what is assumed about the pressure dependence of wind cooling. If the disk becomes thermally unstable, possible outcomes range from a complex 'limit cycle' behavior (e.g., periods of inflow followed by intense rapid burning) to a complete dynamical explosion.

In this series of papers we explore the effect of nuclear burning on the structure and evolution of RIAFs by means of axisymmetric hydrodynamic simulations. In paper I (this work) we explore the general dynamical properties of NuDAFs and their outflows, and compare them to the known case where nuclear burning is absent (e.g., Stone et al. 1999). As in M12, our study focuses on disks created by the tidal disruption of a WD by a NS or BH binary companion, in part because the global properties of the torus are relatively well-constrained by the parameters of the binary. However, many of the conclusions we reach should apply to other similar astrophysical events, such as the collapse of a rotating star.

In this initial study we make several simplifications in order

to clearly identify the processes controlling the dynamics, and to allow an efficient exploration of parameter space. The most important of these approximations is to parameterize the angular momentum transport in the disk by an anomalous shear viscosity. We also adopt an ideal gas equation of state with a single adiabatic index, and for ease include only one nuclear reaction. In a subsequent paper we will use a realistic equation of state (EOS) and extend our nuclear reaction chain to a full α-reaction network, thus enabling a more reliable prediction of observational signatures.

The paper is organized as follows. In §2 we describe the physics included in our model. Details on the numerical implementation are provided in §3. Results are presented in §4, beginning with an overview of a fiducial model, followed by sub-sections on exploding and quiescent models. Implications from our results are discussed in §5, and a bulleted summary of our conclusions is given in §6. Conversion of physical to code units and reaction rates employed are described in Appendix A. Appendix B documents tests of our numerical code. An analytic model for the conditions leading to disk detonation via the Zel'dovich mechanism is provided in Appendix C.

Readers uninterested in technical details are encouraged to skip directly to §4.1.

2. PHYSICAL MODEL

As a clear physical testbed to study NuDAFs, we focus on disks that form when a WD is tidally disrupted by a companion NS or BH in a close binary system. We first review the characteristic properties of these disks, and then discuss the physical approximations made in this study.

2.1. *Disk Properties*

As discussed in Fryer et al. (1999) and M12, whether the WD is disrupted by the primary depends on whether mass transfer is stable or unstable following the onset of Roche lobe overflow. Stability depends on the mass ratio of the binary $q = M_{\rm WD}/M_{\rm c}$, with higher values of $q \gtrsim 0.2-0.5$ favoring disruption (e.g., Paschalidis et al. 2009). Here $M_{\rm WD}$ and $M_{\rm c}$ are the mass of the WD and the central compact object (NS or BH), respectively. Once the WD is disrupted, conservation of angular momentum implies that the material will circularize around the NS/BH at a characteristic radius

$$R_0 = \frac{a_{\rm RLOF}}{1+q}, \tag{1}$$

where

$$a_{\rm RLOF} = R_{\rm WD} \frac{0.6q^{2/3} + \ln(1+q^{1/3})}{0.49q^{2/3}} \tag{2}$$

is the orbital separation at Roche lobe overflow (Eggleton 1983) and $R_{\rm WD}$ is the WD radius. Note that equation (1) neglects the self-gravity of the disk. The WD radius $R_{\rm WD}$ is related to its mass by (Nauenberg 1972; Fryer et al. 1999)

$$R_{\rm WD} \simeq 10^9 \left(\frac{M_{\rm WD}}{0.7M_\odot} \right)^{-1/3} \left[1 - \left(\frac{M_{\rm WD}}{M_{\rm CH}} \right)^{4/3} \right]^{1/2} \left(\frac{\mu_e}{2} \right)^{-5/3} {\rm cm}, \tag{3}$$

where $M_{\rm CH} \simeq 1.45(\mu_e/2)^{-2} M_\odot$ is the Chandrasekhar mass and μ_e is the mean molecular weight per electron. Table 1 gives the circularization radii for models considered in this paper.

As matter circularizes around the NS/BH, a fraction of the kinetic energy of rotation is thermalized. This results in a thick torus (e.g., Fryer et al. 1999) with a scale-height $H_0 \sim R_0/2$ and an average density

$$\bar{\rho} \sim \frac{M_{\mathrm{WD}}}{R_0^3} = 1.5 \times 10^5 \left(\frac{M_{\mathrm{WD}}}{0.6M_\odot}\right)\left(\frac{10^{9.3}\,\mathrm{cm}}{R_0}\right)^3 \mathrm{g\,cm^{-3}}. \quad (4)$$

The orbital time at the circularization radius is

$$t_{\mathrm{orb}} \simeq 40 \left(\frac{R_0}{10^{9.3}\,\mathrm{cm}}\right)^{3/2}\left(\frac{M_{\mathrm{c}}}{1.4M_\odot}\right)^{-1/2} \mathrm{s}. \quad (5)$$

Assuming that the internal energy e_{int} is dominated by non-degenerate particles, and that it balances 25% of the gravitational energy e_{grav} at the circularization radius, one finds a characteristic torus temperature

$$T_{\mathrm{vir}} \simeq 3 \times 10^8 \left(\frac{e_{\mathrm{int}}}{4e_{\mathrm{grav}}}\right)\left(\frac{\mu}{1.75}\right)\left(\frac{M_{\mathrm{c}}}{1.4M_\odot}\right)\left(\frac{10^{9.3}\,\mathrm{cm}}{R_0}\right) \mathrm{K}, \quad (6)$$

where

$$\mu = \left(Y_e + \sum_i \frac{X_i}{A_i}\right)^{-1} \quad (7)$$

is the mean molecular weight, with Y_e the electron fraction, and $\{X_i, A_i\}$ the mass fraction and atomic number of ionic species i, respectively.

The characteristic timescale for matter to accrete may be estimated by the viscous time[5]

$$t_{\mathrm{visc}} \simeq \alpha^{-1}\left(\frac{R_0^3}{GM_{\mathrm{c}}}\right)^{1/2}\left(\frac{H_0}{R_0}\right)^{-2}$$

$$\sim 2600\,\mathrm{s}\left(\frac{0.01}{\alpha}\right)\left(\frac{R_0}{10^{9.3}\,\mathrm{cm}}\right)^{3/2}\left(\frac{1.4M_\odot}{M_{\mathrm{c}}}\right)^{1/2}\left(\frac{H_0}{2R_0}\right)^{-2}, \quad (8)$$

where α parametrizes the disk viscosity (§2.2), resulting in a characteristic accretion rate

$$\dot{M}_0 \sim \frac{M_{\mathrm{WD}}}{t_{\mathrm{visc}}}$$

$$\sim 2 \times 10^{-4} M_\odot\,\mathrm{s^{-1}}\left(\frac{\alpha}{0.01}\right)\left(\frac{M_{\mathrm{WD}}}{0.6M_\odot}\right)\left(\frac{R_0}{10^{9.3}\,\mathrm{cm}}\right)^{-3/2}$$

$$\times\left(\frac{M_{\mathrm{c}}}{1.4M_\odot}\right)^{1/2}\left(\frac{H_0/R_0}{0.5}\right)^2. \quad (9)$$

For the thermodynamic conditions above, the opacity is dominated by electron scattering. The timescale for photons to diffuse out of the disk midplane is then

$$t_{\mathrm{diff}} \simeq \frac{\kappa_{\mathrm{es}}\bar{\rho}}{c}H_0^2 \sim 10^5 \left(\frac{M_{\mathrm{WD}}}{0.6M_\odot}\right)\left(\frac{10^{9.3}\,\mathrm{cm}}{R_0}\right)\left(\frac{H_0/R_0}{0.5}\right)^2 \mathrm{yr}, \quad (10)$$

where κ_{es} is the electron scattering opacity. Note that since t_{diff} is much longer than the timescale for disk formation ($\sim$

---

[5] Note that t_{visc} evaluated at large radii in the disk generally underestimates the true accretion timescale onto the central object since the net accretion rate usually decreases with decreasing radii (e.g., $\dot{M} \propto r$) in most models of RIAFs. Equations (8) and (9) nevertheless represent useful characteristic values.

t_{orb}) or viscous evolution ($\sim t_{\mathrm{visc}}$), this implies that the disk is highly radiatively inefficient and hence radiation losses can be neglected.

We limit our simulations to regions of the disk external to the radius $R_{\mathrm{in}} \sim 10^7$ cm $\sim 0.01R_0$, a choice made primarily for computational expediency. This cutoff is justified because nuclear burning primarily occurs exterior to this radius, with only *endothermic* dissociation happening inside this point (M12).

Neutrinos can in principle also cool the disk. The timescale for neutrino cooling near the disk circularization radius R_0 due to e^-/e^+ pair annihilation is estimated to be $t_\nu \sim 5 \times 10^5$ yr at the fiducial densities and temperatures given in equations (4) and (6), again much longer than the timescale for disk evolution. However, as matter flows inwards to smaller radii where the temperature is higher, neutrino cooling is increasingly important, possibly even causing the disk to transition to a geometrically thin configuration (e.g., Di Matteo et al. 2002). A straightforward calculation shows that a thin disk obtains inside a critical radius R_ν given by (Chen & Beloborodov 2007; see also Metzger et al. 2008, their eq. [11])

$$R_\nu \approx 2 \times 10^5\mathrm{cm} \left(\frac{\dot{M}}{10^{-4}M_\odot\,\mathrm{s^{-1}}}\right)^{6/5}\left(\frac{M_{\mathrm{c}}}{1.4M_\odot}\right)^{-3/5}\left(\frac{\alpha}{0.01}\right)^{-2}. \quad (11)$$

If the characteristic accretion rate near the outer edge of the disk (9) is similar to that at smaller radii in the disk (as may *not* be valid for RIAFs), then from equation (11) one infers that a thin disk is only possible at radii $\ll 10^7$ cm. Although neutrino cooling is unlikely to significantly alter the disk thermodynamics in our computational domain, we nevertheless include this effect in most calculations (§3.3) to compensate for the exclusion of radiation pressure (§2.3).

2.2. *Angular Momentum Transport*

Transport of angular momentum in a fully ionized disk is thought to be mediated primarily via Maxwell stresses associated with the MRI. If the initial magnetic field of the WD is strong and the torus forms with a strong poloidal field, then a magnetocentrifugal wind can also carry away angular momentum (e.g., Blandford & Payne 1982; Stone & Pringle 2001). The interior magnetic fields of WDs are not well constrained observationally, but the measured exterior fields range from $\lesssim 10$ kG in most WDs, up to several hundred MG in a small population of highly magnetized WDs (Wickramasinghe & Ferrario 2000). These fields are much less than the value $\sim 10^{12}$ G that would reach equipartition with the gas pressure in the torus,[6] suggesting that angular momentum loss to winds may be neglected.

Assuming that the magnetic field is weak, the evolution of the torus should resemble that found by previous three dimensional MHD simulations of RIAFs onto black holes at large distances from the event horizon (Hawley et al. 2001; Igumenshchev et al. 2003). Unfortunately, MHD simulations are computationally expensive. One reason is that toroidal magnetic fields amplified by the MRI tend to rise buoyantly into low density regions above the disk midplane (e.g., Davis et al. 2010; Shi et al. 2010). This causes the Alfvén speed to be very large, thus limiting the dynamic range in radii or evolution time that can be explored due to a small Courant-Friedrichs-Lewy (CFL) timestep (Stone & Pringle 2001). This constraint

---

[6] The large-scale field may be amplified somewhat during disk formation via linear field winding, but this is only likely to enhance the toroidal field.

becomes especially severe given the need to resolve the most unstable mode of the MRI for a reliable saturation amplitude (e.g., Hawley et al. 1995).

A less costly alternative, which we adopt, is to perform hydrodynamic simulations with a suitably chosen anomalous shear stress. There are obvious caveats to this approach. First, the MRI converts orbital kinetic energy directly into turbulent magnetic and kinetic energy, with the ensuing stresses being responsible for the transport of angular momentum. In contrast, viscous heating converts orbital energy into heat, which then drives convection through entropy gradients (Hawley et al. 2001). This causes the hydrodynamic models to achieve a state of marginal convective stability (Stone et al. 1999), whereas in MHD the very same stability criterion must be violated in order for the MRI to operate (Hawley et al. 2001). The relative spatial distribution of specific angular momentum and entropy thus differs between the hydrodynamic and MHD cases. In addition, the spatial and temporal distribution of heating is very different between MRI-driven magnetohydrodynamic turbulence and shear viscosity (e.g., Hirose et al. 2006). This could potentially alter the thermodynamic structure of the disk and hence the spatial distribution of nuclear burning.

Despite these caveats, purely hydrodynamic simulations capture important aspects of MHD simulations. First, the time-averaged mass fluxes in the disk midplane have the same qualitative form, with strong inflow and outflow nearly canceling each other out, resulting in a net accretion rate that is approximately constant with radius (Stone et al. 1999; Stone & Pringle 2001; Hawley et al. 2001). Second, the radial scalings of time-averaged quantities (e.g., density and temperature) found by MHD simulations can be matched by hydrodynamic simulations if the functional form of the shear stress is suitably chosen (Stone & Pringle 2001). These scalings do not differ substantially between two- and three dimensions (Hawley et al. 2001).

The experimental approach of this study demands the ability to simulate accretion torii over a large dynamic range in spatial distances and timescales. We thus begin our study of NuDAFs by performing hydrodynamic simulations with an anomalous viscous stress. A similar approach was adopted recently by Schwab et al. (2012) in studying the evolution of accretion disks created by WD-WD mergers. In order to best evaluate the uncertainties introduced by this approach, we adopt several functional forms for the kinematic viscosity, each of which lead to different transient and quasi-steady-state outcomes.

The first parameterization is that which makes the ratio of viscous to orbital times independent of radius,

$$\nu_{\rm ct} = \tilde{\nu}_0 \sqrt{GM_{\rm c}R_0} \left(\frac{r}{R_0} \right)^{1/2}, \qquad (12)$$

where $\tilde{\nu}_0$ is a dimensionless constant. This form was found by Stone et al. (1999) to yield a self-similar behavior in the inner regions of the disk, with $\rho \propto r^{-1/2}$ and $T \propto r^{-1}$. The relationship between $\tilde{\nu}_0$ and the ratio of timescales is

$$\tilde{\nu}_0 \simeq 1.6 \times 10^{-3} \left[\frac{t_{\rm visc}/t_{\rm orb}}{100} \right]. \qquad (13)$$

We employ this prescription to compare with analytic expectations for the dynamical importance of burning (§2.3).

We also employ a Shakura & Sunyaev (1973) parameterization

$$\nu_\alpha = \alpha \frac{c_s^2}{\Omega_K}$$
$$= \alpha \left(\frac{c_s^2}{GM_{\rm c}/r} \right) \sqrt{GM_{\rm c}R_0} \left(\frac{r}{R_0} \right)^{1/2} \qquad (14)$$

where Ω_K is the Keplerian frequency and $c_s^2 = \gamma p/\rho$ is the adiabatic sound speed. The functional form of ν_α differs from $\nu_{\rm ct}$ in the additional dependence on the ratio of thermal to gravitational energies. At the circularization radius, the numerical value of $\tilde{\nu}_0$ in equation (13) corresponds to $\alpha \sim 0.01$, with exact values depending on the thermal content of the disk.

Finally, to connect with MHD calculations, we employ the prescription of Stone et al. (1999)

$$\nu_{\rm spb} = \tilde{\nu}_0 \sqrt{GM_{\rm c}R_0} \left(\frac{\rho}{\rho_1} \right), \qquad (15)$$

where ρ_1 is a reference density, taken to be the maximum value in the initial condition (§3.2). This parameterization yields radial scalings in agreement with axisymmetric MHD simulations with low initial poloidal fields (Stone & Pringle 2001).

Following Stone et al. (1999), we include only the azimuthal components of the viscous stress tensor $\mathbb{T}$ in our simulations.

$$T_{r\phi} = \rho\nu \, \frac{r}{\sin\theta} \frac{\partial}{\partial r} \left(\frac{\ell_z}{r^2} \right) \qquad (16)$$

$$T_{\theta\phi} = \rho\nu \, \frac{\sin\theta}{r^2} \frac{\partial}{\partial\theta} \left(\frac{\ell_z}{\sin^2\theta} \right). \qquad (17)$$

Including all components of the stress would make the fluid truly viscous, and suppress convection in the poloidal direction (e.g., Igumenshchev & Abramowicz 1999). Our simulations, like previous hydrodynamic studies, mimic turbulent angular momentum transport via thermally-driven convection. Suppressing this effect would suppress the very mechanism that gives plausibility to a hydrodynamic modeling.

Given the potentially large mass of the disrupted WD relative to that of the central NS/BH, it is also possible that the disk will be susceptible to gravitational instabilities, which could contribute to the transport of angular momentum via spiral density waves (e.g., Larson 1984). We neglect this possibility here, since pressure waves may stabilize such instabilities (the disk is quasi-virial and geometrically thick). Also, our analysis does not include self-gravity. However, to the extent that such waves are present and transport angular momentum outwards, some of the qualitative effects of self-gravity may be captured by our prescription for angular momentum transport.

2.3. Microphysics

For a given initial composition of the torus, we focus on the reaction activated first at large radii in the disk, since energy input from this reaction is the most important relative to the local rate of viscous heating (M12).

We focus mostly on the reaction $^{12}{\rm C}(^{12}{\rm C},\gamma)^{24}{\rm Mg}$, relevant to disks formed from mid-mass C-O WDs. We also calculate a few models that use the triple-alpha reaction, as would be appropriate for disks arising from low-mass He WDs or He stars. Our analysis is also applicable to α–capture reactions [e.g., $^4{\rm He}(^{16}{\rm O},\gamma)^{20}{\rm Ne}$], which are relevant for a hybrid

He-C-O WD disk or to the outer layers of a collapsing Wolf-Rayet star (Woosley & Heger 2006). We exclude the parameter regime relevant to massive WDs with O-Ne composition, because the small circularization radii R_0 (eq. [1]) and high disk temperatures T_{vir} (eq. [6]) suggest that in these systems burning begins during the circularization process itself (M12).

To better enable analytic comparisons, we adopt a generic power-law form for the $^{12}C(^{12}C,\gamma)^{24}Mg$ reaction rate

$$\dot{X}_f = -AX_f^2 \rho T^\beta, \qquad (18)$$

where X_f is the mass fraction of fuel (carbon), A is a normalization constant, and β results from expanding the analytic expression for the reaction rate as a Taylor series in temperature (e.g., Kippenhahn & Weigert 1994) about the point at which the burning time and dynamical time (or viscous time) are comparable in the disk midplane. In the temperature range $(0.6 - 1.2) \times 10^9$ K, this procedure yields $\beta = 29$. In some of our models we employ the full functional form of each reaction (Caughlan & Fowler 1988), suitably converted to code units given the parametric equation of state. Details of this procedure are given Appendix A.

Associated with each reaction is the specific nuclear binding energy released,

$$\varepsilon_{nuc} = QX_f/m_a, \qquad (19)$$

where Q is the total energy released per reaction and m_a is the mass of the reaction product. In several simulations we artificially suppress the value of $Q \propto \varepsilon_{nuc}$ from its true physical value Q_0 in order to explore how the outcome of NuDAF evolution depends the amount of nuclear energy released.

For simplicity, we use an ideal gas equation of state with a single adiabatic index $\gamma = 5/3$. As shown in M12, gas pressure exceeds radiation pressure close to the disk midplane during phases of evolution when most of the mass accretes (i.e. on timescales $t \gtrsim t_{visc}$). However, radiation pressure contributes an increasingly larger fraction of the total pressure at smaller radii in the disk. It dominates over gas pressure when the density is low at early times prior to when the accretion rate achieves a steady-state. Neglecting radiation pressure results in an overestimate of the temperature (and hence the rate of nuclear reactions), potentially producing unphysical prompt detonations in some of our simulations, an issue we discuss further in §4.2. For completeness, we also include neutrino cooling as parameterized by Itoh et al. (1996).[7]

3. NUMERICAL METHOD

3.1. *Equations Solved*

Spherical polar coordinates in axisymmetry (r, θ) are adopted, with the origin at the center of the neutron star. We solve the equations of mass, momentum, energy, and chemical species conservation, with source terms due to gravity, shear viscosity, and nuclear reactions:

$$\frac{\partial \rho}{\partial t} + \nabla \cdot (\rho \mathbf{v}_p) = 0 \qquad (20)$$

$$\frac{d\mathbf{v}_p}{dt} = \mathbf{f}_c - \frac{1}{\rho}\nabla p - \frac{GM_c}{r^2}\hat{r} \qquad (21)$$

$$\rho \frac{d\ell_z}{dt} = r\sin\theta \, (\nabla \cdot \mathbb{T})_\phi \qquad (22)$$

$$\rho \frac{de_{int}}{dt} + p\nabla \cdot \mathbf{v}_p = \frac{1}{\rho\nu}\mathbb{T} : \mathbb{T} + \rho \left(\dot{Q}_{nuc} - \dot{Q}_{cool} \right) \qquad (23)$$

---
[7] http://cococubed.asu.edu/code_pages/codes.shtml

$$\frac{dX_f}{dt} = \dot{X}_f = -\frac{\dot{Q}_{nuc}}{Q/m_f}, \qquad (24)$$

where ρ, p, $\mathbf{v}_p = v_r\hat{r} + v_\theta\hat{\theta}$, and e_{int} are the fluid density, pressure, poloidal velocity, and internal energy, respectively, and $d/dt \equiv \partial/\partial t + \mathbf{v}_p \cdot \nabla$ is the Lagrangian differential operator.

The specific angular momentum along the symmetry axis satisfies $\ell_z = r\sin\theta v_\phi$, with v_ϕ the azimuthal velocity. The corresponding centrifugal force in the poloidal direction is

$$\mathbf{f}_c = \frac{\ell_z^2}{r^3 \sin^3\theta}\left[\sin\theta\hat{r} + \cos\theta\hat{\theta} \right]. \qquad (25)$$

The system of equations (20)-(24) is closed with an ideal gas equation of state with adiabatic index $\gamma = 5/3$, so that $p = (\gamma - 1)\rho e_{int}$. The nuclear abundances are constrained by baryon number conservation, $X_f + X_a + X_x = 1$, where X_a and X_x denote the mass fractions of ash and inert species, respectively. The nuclear energy generation rate $\dot{Q}_{nuc}$ is given by one of the full reaction rates described in Appendix A, or by a power-law approximation using equations (18) and (24). $\dot{Q}_{cool}$ is the neutrino energy loss rate per unit mass.

Throughout this paper, we express quantities in terms of the Keplerian velocity at the circularization radius $v_{k0} = (GM_c/R_0)^{1/2}$, and the orbital time at the same location, $t_{orb} = 2\pi R_0^{3/2}/(GM_c)^{1/2}$.

3.2. *Initial Conditions*

The initial condition is a constant entropy and specific angular momentum torus (e.g., Papaloizou & Pringle 1984) with uniform chemical composition. A realistic merger will produce a torus with a more general radial distribution of angular momentum, since the disruption process is not instantaneous (e.g., Fryer et al. 1999). We ignore this complication in the interest of clarity. The implications of this assumption in light of our results are discussed in §5.1.

Following Stone et al. (1999), the torus density is normalized to its maximum value ρ_{max}, thereby fixing the polytropic constant in terms of the adiabatic index and the torus distortion parameter d. The resulting initial density distribution is

$$\left(\frac{\rho}{\rho_{max}} \right)^{\gamma-1} = \frac{2d}{d-1}\left[\frac{R_0}{r} - \frac{1}{2}\left(\frac{R_0}{r\sin\theta} \right)^2 - \frac{1}{2d} \right]. \qquad (26)$$

The distortion parameter d is a measure of the internal energy content of the torus. The maximum ratio of internal to gravitational energy occurs at the point of maximum density $(r = R_0, z = 0)$,

$$\frac{e_{int,max}}{GM/R_0} = \frac{1}{2\gamma}\frac{d-1}{d}. \qquad (27)$$

Given the angular momentum distribution $j(r)$ of the torus, the value of d is in principle fully determined by the properties of the disrupted binary and energy conservation. Unfortunately, the uncertainty in $j(r)$ and the complication of self-gravity (which is not included in the initial torus solution) impede a precise determination of d. In the absence of more detailed information, we adopt $d = 1.5$ as a fiducial value for most of our models. For $\gamma = 5/3$, this yields a maximum ratio of internal to gravitational energy (eq. [27]) of 10%. We also use $d = \{1.2, 3\}$ in some models, to study the sensitivity of our results to this choice. The integrated mass distributions so obtained bracket the results of Fryer et al. (1999) for WD-BH disks.

A physical temperature is obtained by assuming that the pressure is provided by a non-relativistic ideal gas, and using a mean molecular weight (eq. [7]) appropriate to the initial WD composition. Similarly, a physical density is obtained by multiplying the average disk density (eq. [4]) by the ratio of the maximum to average density in the initial torus. This ratio is a function of d and γ only. Details of this unit conversion are provided in Appendix A.

The torus is surrounded by a low-density isothermal atmosphere,

$$\rho_{\mathrm{at}}(r) = \rho_{\mathrm{at},0} \exp\left\{ \frac{GM}{c_{\mathrm{at}}^2 r_{\mathrm{in}}} \left(\frac{r_{\mathrm{in}}}{r} - 1 \right) \right\}, \qquad (28)$$

where r_{in} is the inner radial boundary of the computational domain, and $c_{\mathrm{at}}^2 = p_{\mathrm{at},0}/\rho_{\mathrm{at},0}$ is the isothermal sound speed of the atmosphere. This surrounding medium has the advantage of being stably-stratified. We find that a constant density atmosphere, such as that used by Stone et al. (1999), generates excessive numerical noise near the inner boundary. The normalization constant is chosen to be much smaller than the bulk of the torus density, and an order of magnitude below the density at which we cut off source terms (3.3). At radii $r \gg r_{\mathrm{in}}$, the density asymptotes to $\rho_\infty = \rho_{\mathrm{at}} \exp[-GM/(c_{\mathrm{at}}^2 r_{\mathrm{in}})]$. In most models, we adopt $\rho_{\mathrm{at},0}/\rho_{\mathrm{max}} = 10^{-6}$ and $c_{\mathrm{at}}^2 = 25 GM_c/R_0$. The temperature is chosen so that the resulting density scale height at the inner boundary is resolved with at least 5 cells in radius. This choice of atmospheric parameters causes a negligible effect on the torus evolution even though the atmosphere itself is unbound. In a few models, we increase the background density to $\rho_{\mathrm{at},0}/\rho_{\mathrm{max}} = 10^{-4}$ to obtain smoother evolution of the inner edge of the torus during the initial infall. This higher value artificially slows down ejected material, however, and is kept for comparison purposes only.

3.3. *Time-dependent evolution*

We use FLASH3.2 (Dubey et al. 2009) to evolve the system of equations (20)-(24) with the dimensionally-split version of the Piecewise Parabolic Method (PPM, Colella & Woodward 1984). The public version of the code has been modified to allow for a non-uniformly spaced grid in spherical polar coordinates as described in Fernández (2012).

The specific angular momentum is included as an advected scalar subject to viscous source terms (eq. [22]). To take advantage of the finite-volume character of the hydrodynamic method, the diffusion operator is recast as

$$r \sin\theta \, (\nabla \cdot \mathbb{T})_\phi = \nabla \cdot \mathbf{F}_\ell, \qquad (29)$$

where

$$\mathbf{F}_\ell = r \sin\theta \left(T_{r\phi} \hat{r} + T_{\theta\phi} \hat{\theta} \right) \qquad (30)$$

is the angular momentum flux vector. This diffusive flux is added to the advective flux obtained from the Riemann problem solution at each cell interface. The combined flux is then used to update the volume-averaged value of ℓ_z (see Lindner et al. 2010 for a similar implementation in cylindrical coordinates). The internal energy is updated by simple operator-split addition of the scalar viscous energy generation rate (equation 23). Numerical stability requires the evolution time step to be lower than

$$\Delta t_{\mathrm{visc}} = \frac{1}{2} \min\left(\frac{\Delta r^2}{\nu}, \frac{r^2 \Delta \theta^2}{\nu} \right), \qquad (31)$$

where the minimization is carried out over the entire computational domain. This constraint on the time step is imposed in addition to the CFL condition required by the hydrodynamic method. The centrifugal force is included as part of the default treatment of 'fictitious' forces that arise in curvilinear coordinates.

By default, FLASH3.2 evolves the total specific energy (internal plus kinetic). To avoid adding the additional source terms needed to account for the Eulerian rate of change of the rotational kinetic energy, we only evolve internal energy (equation 23).

The nuclear energy generation rate and neutrino cooling are also included via simple operator-split update of the internal energy. We suppress nuclear burning inside shocks, and employ a standard treatment of multi-species advection (Plewa & Müller 1999). To avoid artificial thermonuclear runaways, we impose an additional constraint on the time-step from nuclear burning

$$\Delta t_{\mathrm{nuc}} = 0.8 \frac{e_{\mathrm{int}}}{\dot{Q}_{\mathrm{nuc}}}. \qquad (32)$$

In practice, the simulation time-step is dominated by the CFL condition given the atmospheric temperature and the grid resolution, being usually 10 to 100 times smaller than Δt_{nuc}.

The computational grid is logarithmically spaced in the radial direction, covering four orders of magnitude in length. In most cases, it extends from $r_{\mathrm{min}} = 0.01 R_0$ to $r_{\mathrm{max}} = 100 R_0$, although a few models use a smaller inner radius (Table 1). In the polar direction the grid covers the full range of latitudes ($[0°, 180°]$), with cells having a constant ratio of sizes (e.g., Stone & Norman 1992). We make this spacing symmetric relative to the equator, with the coarsest cells next to the polar axis. Our standard resolution is $N_r = 64$ cells per decade in radius. The angular spacing is chosen so that $\Delta\theta \simeq \Delta r/r \simeq 2°$ at the equator, and $\Delta\theta_p = 4°$ or $6°$ next to the polar axis[8]. We evolve one model at higher resolution, with $N_r = 128$ cells per decade in radius, $\Delta\theta \simeq \Delta r/r \simeq 1°$ at the equator, and $\Delta\theta_p = 2°$.

The boundary conditions at the polar axis are reflecting in all variables. At the inner radial boundary, we impose a zero-gradient boundary condition for the mass flux, subtracting the contribution from the isothermal atmosphere. For a ghost cell with position (r, θ), the density, pressure, and radial velocity are set to

$$\rho(r,\theta) = \rho(r_1, \theta) - \rho_{\mathrm{at}}(r_1) + \rho_{\mathrm{at}}(r) \qquad (33)$$
$$p(r,\theta) = p(r_1, \theta) - p_{\mathrm{at}}(r_1) + p_{\mathrm{at}}(r) \qquad (34)$$
$$v_r(r,\theta) = \left(r_1/r \right)^2 v_r(r_1, \theta) \qquad (35)$$

if $v_r(r_1, \theta) < 0$ and $\rho(r_1, \theta) > \rho_{\mathrm{at}}(r_1)$, where r_1 is the radial coordinate of the center of the first active cell outside the inner radial boundary. Otherwise the radial velocity in the ghost cells is set to zero. Because fluid elements associated with the disk normally have densities much larger than that of the atmosphere, this is in effect a standard outflow boundary condition. The additional terms ensure that the isothermal atmosphere remains quiescent when no material is accreted. The ghost cells for the internal energy are set in consistency to those of the density and pressure. All other variables are given a zero radial gradient in the ghost cells. This prescription is repeated at the outer radial boundary, with the only modifica-

---

[8] We find that the funnel that develops around the rotation axis can cause numerical problems if the angular resolution is too fine.

TABLE 1
MODELS EVOLVED

Model	$M_{\rm WD}$ ($M_\odot$)	$X_{\rm He}/X_{\rm C}/X_{\rm O}$[a]	d[b]	Reaction[c]	Q/Q_0[d]	Visc.[e]	$\tilde{\nu}_0, \alpha$[f]	N_r[g]	$\theta_{\rm p}$[h]	$r_{\rm in}/R_0$ ($M_\odot$)	R_0 (cm)	ρ_∞[i] ($\rho_{\rm max}$)	ρ_0[j] ($\rho_{\rm max}$)	ν Cool?
COq000	0.6	0/0.5/0.5	1.5	power-law	0.00	ct	0.0016	64	4	10^{-2}	$10^{9.3}$	$10^{-5.7}$	10^{-3}	Yes
COq010					0.10									
COq025					0.25									
COq050					0.50									
COq075					0.75									
COq100					1.00									
COq000_nc	0.6	0/0.5/0.5	1.5	power-law	0.00	ct	0.0016	64	4	10^{-2}	$10^{9.3}$	$10^{-7.7}$	10^{-3}	No
COq010_nc					0.10									
COq025_nc					0.25									
COq050_nc					0.50									
COq100_nc					1.00									
COq050_HR	0.6	0/0.5/0.5	1.5	power-law	0.50	ct	0.0016	128	2	10^{-2}	$10^{9.3}$	$10^{-5.7}$	10^{-3}	Yes
COq050_at								64	4			$10^{-7.7}$		
COq050_ρ_0													10^{-4}	
COq050_dL			1.2										10^{-3}	
COq050_dH			3.0						6					
COq050_νH			1.5					0.016						
COq050_spb						spb	0.008		4					
COq050_α						α	0.0144							
CO_f1	0.6	0/0.5/0.5	1.2	^{12}C+^{12}C	1.00	ct	0.016	64	4	10^{-2}	$10^{9.3}$	$10^{-7.7}$	10^{-3}	Yes
CO_f2			1.5				0.0016							
HE_00	0.3	1/0/0	1.5	3α	0.00	ct	0.016	64	4	$10^{-2.5}$	$10^{9.6}$	$10^{-11.8}$	10^{-3}	Yes
HE_f1					1.00									

[a] Initial mass fractions of helium, carbon, and oxygen, respectively.
[b] Distortion parameter controlling the initial thermal content of the torus (see eq. [27]).
[c] Nuclear reaction rate employed (Appendix A).
[d] Ratio of the nuclear energy released per reaction Q to the true physical value Q_0.
[e] Functional form of the kinematic viscosity (eqs. [12]-[15]).
[f] Magnitude of viscosity $\tilde{\nu}_0$ or α, as appropriate. The coefficient α is related to $\tilde{\nu}_0$ through equation (27).
[g] Number of cells per decade in radius.
[h] Angular resolution at the polar axis
[i] Asymptotic atmospheric density (eq. [28]).
[j] Cutoff density for source terms (eq. [36]).

tion being a reversal of the required sign of the radial velocity for outflow.

To prevent excessive heating in regions of low density, we multiply all the energy and viscous source terms by a cutoff function $f(\rho)$. Otherwise the CFL timestep can become prohibitively short in regions that are unimportant for the disk evolution. The functional form of the cutoff is

$$ f(\rho) = \begin{cases} 1 & \rho > \rho_0 \\ e^{(-\rho_0/\rho)} & \rho \leq \rho_0, \end{cases} \qquad (36) $$

where ρ_0 is a fiducial density, which we choose to be $\rho_0/\rho_{\rm max} = 10^{-3}$. In the initial torus configuration, 99.99% of the mass is included inside this contour. We have verified that the evolution of the relevant dynamic quantities is not very sensitive to the value of this cutoff below a certain value (§3.4). Although a low-density suppression of burning may seem ad hoc, it can be motivated physically. First, at low densities our assumed ideal gas EOS overestimates the true temperature (and hence burning rate), since we have neglected the effects of radiation pressure, which dominates the total pressure in low density regions. Also, in low density regions the photon optical depth may become sufficiently small that radiative cooling (also neglected in our simulation) may become relevant on the timescales of interest.

Numerical tests of the angular momentum evolution are presented in Appendix B.

3.4. Models Evolved

We evolve a suite of models that systematically sample the parameter space of disk properties relevant to WD-NS mergers. The complete set is shown in Table 1.

Models are grouped according to the parameter being varied. Most cases focus on a C-O WD of mass $M_{\rm WD} = 0.6M_\odot$ accreting onto a NS of mass $M_c = 1.4M_\odot$. The composition is 50% carbon and 50% oxygen. The first two subsets of models focus on the effect of varying the energy released per nuclear reaction Q, expressed as a fraction of its true physical value Q_0, using the power-law approximation to the ^{12}C(^{12}C,γ)^{24}Mg reaction (eq. [18]). One sequence includes neutrino cooling and the other does not (models ending in _nc).

As we discuss below, most of our models with $Q \geq 0.5Q_0$ undergo large-scale detonations, while those with $Q < 0.5Q_0$ instead undergo quiescent burning. Since one of our goals is to understand what conditions are necessary for detonation, we adopt the marginal case of the sequence with cooling (COq050) for further parameter variation. The third subset of models thus explores the effect of higher resolution (COq050_HR), torus distortion parameter (COq050_dL and COq050_dH), strength (COq050_νH) and functional form
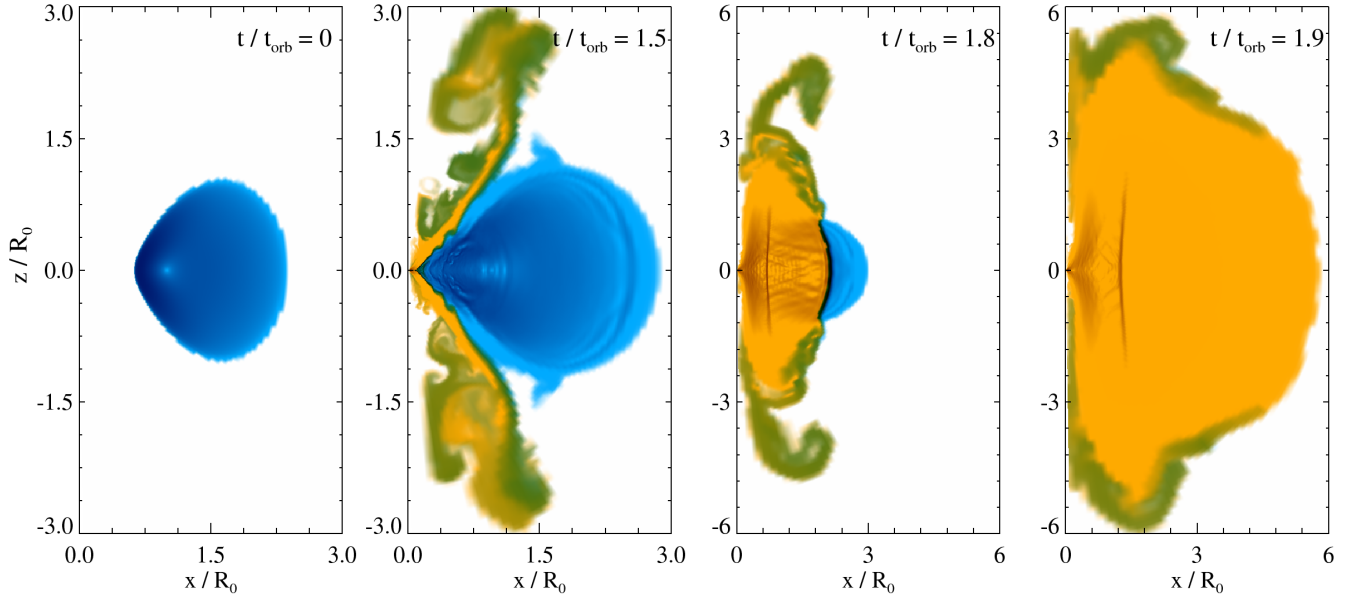
FIG. 1.— Snapshots of model COq050_HR, illustrating the main evolutionary stages of the accretion of a tidally disrupted $0.6M_\odot$ C-O WD onto a $1.4M_\odot$ NS in a case that leads to a detonation. The mass fractions of fuel (carbon) and ash (magnesium) are shown in blue and yellow, respectively, with green regions indicating mixed material. The shading is proportional to the density gradient. From left to right, panels correspond to (a) the initial condition; (b) establishment of a steady burning front at $r_{nuc} \sim 0.1R_0$ (eq. [39]); (c) initiation of detonation; and (d) shock expansion and partial unbinding of the torus. Time is shown in units of the orbital time at $r = R_0$. Note that the spatial scale is enlarged in the final two panels. An animated version of this figure is available in the online version of the article.

(COq050_spb and COq050_α) of the shear stress, magnitude of the atmospheric density (COq050_at), and value of the cut-off density ρ_0 (COq050_ρ0) on the marginal model.

The fourth subset of models employs the full reaction rates to assess the likelihood of detonation in disks formed from C-O and He WDs. Model CO_f1 employs the same parameters as our fiducial C-O WD marginal model, but with the full strength of the energy release ($Q = Q_0$). Model CO_f2 decreases d and increases $\tilde{\nu}_0$ to increase the chance of explosion. Models He_000 and He_f1 explore the evolution of pure He disks ($X_{He} = 1$) under the influence of the triple-alpha reaction. Parameters correspond to a $M_{WD} = 0.3M_\odot$ WD accreting onto a NS of mass $M_c = 1.4M_\odot$. The viscosity is chosen large, to maximize the likelihood of a detonation. The inner boundary of the domain is chosen smaller than in the C-O case, because the ratio of burning to circularization radii is expected to be smaller as well (M12).

4. RESULTS

We begin the presentation of our results with a basic overview (§4.1) of the impact of nuclear burning on the evolution of the accretion disk, focusing on a model which detonates. Then, in separate sections, we elaborate on exploding (§4.2) and quiescent cases (§4.3). The results of our simulations are summarized in Table 3.

4.1. *Overview*

In the absence of nuclear burning, the disk evolves in a way similar to that in the axisymmetric simulations of RIAFs by Stone et al. (1999). The initial torus develops a radial velocity through the action of viscous stresses. Material near the inner edge of the disk reaches the inner boundary within the first few orbital periods as measured at $r = R_0$. As more of the disk spreads inward, viscous heating drives convective turbulence, resulting in inward and outward mass fluxes of comparable

magnitude. Material is ejected in a wide funnel around the rotation axis, but most of the ejecta has negative energy and eventually falls back to the disk. The accretion rate peaks on a timescale which is comparable to a viscous time at $r = R_0$, before gradually decreasing with time thereafter. The properties of torii without burning are discussed in relation to quiescent NuDAFs in §4.3.

The dynamical importance of nuclear energy generation at a given radius can be quantified by the ratio of the specific nuclear energy released per reaction ε_{nuc} (eq. [19]) to the local gravitational binding energy. Given the steep temperature dependence of most reactions, fuel depletion and energy deposition are generally concentrated in a narrow surface that crosses the midplane at a characteristic radius r_{nuc} from the central object. If burning occurs subsonically, the magnitude of the density jump across the burning region is given by the ratio of ε_{nuc} to the specific enthalpy of the fluid w (Landau & Lifshitz 1987; see also Appendix C). The latter is related to the specific gravitational binding energy by a factor $\propto (H/r)^2$ (e.g., M12). Hence, one can use the ratio of ε_{nuc} to w evaluated at $r = r_{nuc}$,

$$\Psi = \frac{\varepsilon_{nuc}}{w(r_{nuc})} \tag{37}$$

$$= \frac{2d}{d-1} \frac{\varepsilon_{nuc}}{GM_c/R_0} \left(\frac{r_{nuc}}{R_0}\right)^m \tag{38}$$

to parameterize the importance of nuclear reactions on the disk evolution. Note that equation (38) is specific to our initial conditions (§3.2); it assumes that the temperature has a power-law dependence with radius, $T \propto r^{-m}$, and makes use of equation (27) for normalization. The values of Ψ quoted in our results below are calculated using an angle-averaged value of $w(r_{nuc})$ obtained directly from our simulations. Equation (38) is a reference value only.

The location of r_{nuc} can be estimated by equating the dy-

TABLE 2
DYNAMICAL IMPORTANCE OF NUCLEAR REACTIONS IN RIAFs.[a]

Reaction	Q_0 (MeV)	$X_{He}/X_C/X_O$[b]	r_{nuc}[c] (10^8 cm)	Ψ[d]
$^{12}C(^{12}C,\gamma)^{24}Mg$	13.93	0.0/0.5/0.5	1.9	1.68
$^{12}C(\alpha,\gamma)^{16}O$	7.16	0.2/0.5/0.3	2.5	1.74
$^{16}O(\alpha,\gamma)^{20}Ne$	4.73	0.2/0.3/0.5	5.1	1.86
$^{16}O(^{16}O,\gamma)^{32}S$	16.54	0.0/0.5/0.5	1.0	0.78

[a] Assuming a geometrically thick, virialized torus with $R_0 = 10^{9.3}$ cm; $\rho \propto r^{-1/2}$ ($\dot{M} \propto r$); viscosity parameter $\alpha = 0.01$; $H/r = 0.3$, and $M_c = 1.4M_\odot$.
[b] Initial mass fractions
[c] Burning radius at which half the initial fuel is consumed. Its value is calculated numerically using the full functional form of the reaction rate.
[d] Ratio of ε_{nuc} to the enthalpy $w = (\gamma - 1)^{-1}(H/r)^2 GM_c/r_{nuc}$ of the flow (eq. [37]).

namical time r/v_{k0} to the nuclear burning time $e_{int}/\dot{Q}_{nuc}$. If the timescale for viscous heating is long compared to that for vertical hydrodrostatic balance (the sound crossing time), then the disk temperature T approaches its virialized value $T_{vir} \propto r^{-1}$ (eq. [6]). Otherwise it has a more general dependence $T \propto r^{-m}$. If the density scales as a power-law with radius $\rho \propto r^n$, then using the power-law approximation to the $^{12}C(^{12}C,\gamma)^{24}Mg$ reaction (eq. [18]), and the power-law form for the viscosity prescription (eq. [12]), one finds that

$$\frac{r_{nuc}}{R_0} \simeq \left[\left(\frac{\varepsilon_{nuc}}{e_{int}} \right) \left(\frac{R_0}{v_{k0}} \right) A X_f \rho_0 T_0^\beta \right]^{1/(m[\beta-1]+n-3/2)} \quad (39)$$

where the zero subscripts on thermodynamic quantities denote their values at $r = R_0$. For C-O torii with $M_{WD} = 0.6M_\odot$, $M_c = 1.4M_\odot$, and $d = 1.5$, we find $r_{nuc}/R_0 \simeq 0.1$, for $m = 1$, and $n = 2$. Equation (39) is sensitive to the radial dependences of the temperature and density, as well as to the temperature normalization at the circularization radius. The position of r_{nuc} will thus change in time as the disk approaches a quasi steady-state configuration.

Assuming a carbon mass fraction $X_C = 0.5$ in ε_{nuc}, a value of $r_{nuc} \simeq 0.1$ yields $\Psi \simeq 1.8(Q/Q_0)$ for the power-law burning rate and a central mass $M_c = 1.4M_\odot$. Using the full functional form for the reaction rate requires solving for r_{nuc}/R_0 numerically. Table 2 shows the result of such a calculation for $^{12}C(^{12}C,\gamma)^{24}Mg$ and other relevant reactions (e.g., α-captures). Note that Ψ is similar in all cases except for oxygen burning, which is lower by a factor ~ 2.

The qualitatively new behavior introduced by nuclear burning is illustrated in Figure 1, which shows several snapshots in the evolution of the C-O torus in our fiducial high resolution model COq050_HR with $Q = 0.5Q_0$ ($\Psi \simeq 0.6$ measured at the moment of final detonation, see Table 3). Initially, the disk is composed entirely of fuel (carbon). During the first orbital period of evolution, the inner edge of the disk moves inwards and increases in temperature, before igniting at some radius initially smaller than the fiducial burning radius r_{nuc}. A narrow burning front is established which moves outwards and then settles at $r \approx r_{nuc}$ on a (local) dynamical time. Turbulence is generated outside of the burning front, triggering a thermonuclear runaway and detonation at the time $t = 1.67t_{orb}$.

After a time $t = 1.9t_{orb}$, the detonation has successfully propagated out through the entire torus. At this point approximately 99% of the initial WD mass ($\sim 0.6M_\odot$) has become unbound. The net energy in this material is $E_{ej} \simeq 3 \times 10^{50}$
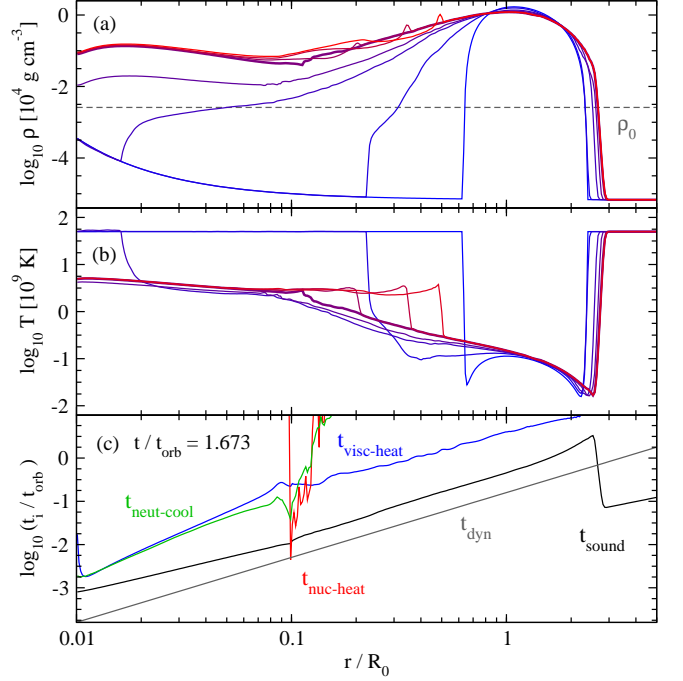

FIG. 2.— *Panels (a) and (b):* Angle-averaged density ρ and temperature T as a function of radius for the model COq050_HR (Fig. 1), respectively. Averages are density-weighted and taken within 45 degrees of the equator. From blue to red, solid curves correspond to times $t/t_{orb} = \{0, 0.5, 1, 1.2, 1.673, 1.68, 1.69, 1.7\}$. The horizontal dashed gray line shows the cutoff density ρ_0 below which nuclear burning is artificially suppressed (eq. [36]). *Panel (c):* Various timescales in the disk as a function of radius at the time $t/t_{orb} = 1.673$ just prior to detonation (compare with Fig. 3). Timescales t_i shown include: dynamical $t_{dyn} = r/v_k(r)$ (grey); sound crossing $t_{sound} = r/c_s$ (black); viscous heating $t_{visc-heat} = e_{int}/\dot{Q}_{visc}$ (blue); nuclear burning $t_{burn-heat} = e_{int}/\dot{Q}_{nuc}$ (red); and neutrino cooling $t_{neut-heat} = e_{int}/\dot{Q}_{cool}$ (green).

ergs, and has a mass-weighted radial velocity of $\bar{v}_{ej} \simeq 6000$ km s^{-1}. A fraction 5% of this mass becomes bound and remains as a remnant disk. In §5 we discuss the possible observational signatures of this supernova-like explosion.

Our calculations show that detonations can occur in NuDAFs ranging from *microexplosions* (e.g., Lisewski et al. 2000) which remain localized, to complete consumption of the initial disk. A large-scale detonation capable of unbinding the disk, and occurring within the first few orbital periods of evolution, appears to be a robust outcome if Ψ is above a critical value $\Psi_{crit} \sim 1$. A primary cause of such detonations is that the shape of the initially stationary burning front is distorted due to the effects of the Rayleigh-Taylor (RT) instability (e.g., Bell et al. 2004) and convective turbulence in the surrounding fluid. In Appendix C we argue that the mixing of fuel and ash due the convective motions present in RIAFs is indeed sufficient for a detonation to occur via the Zel'dovich gradient mechanism (Zel'dovich et al. 1970) if Ψ has the appropriate magnitude.

If $\Psi \ll \Psi_{crit}$, then large scale detonations do not develop and accretion remains relatively steady across the burning front. During this 'quiescent' mode of NuDAF evolution, some fraction of the ash behind the burning front is accreted, while the rest is ejected into an outflow along the polar axis. Even when a detonation does not occur, NuDAFs produce a more powerful outflow than in otherwise identical RIAFs without nuclear burning. The fraction of the material which is gravitationally unbound versus that being accreted is found
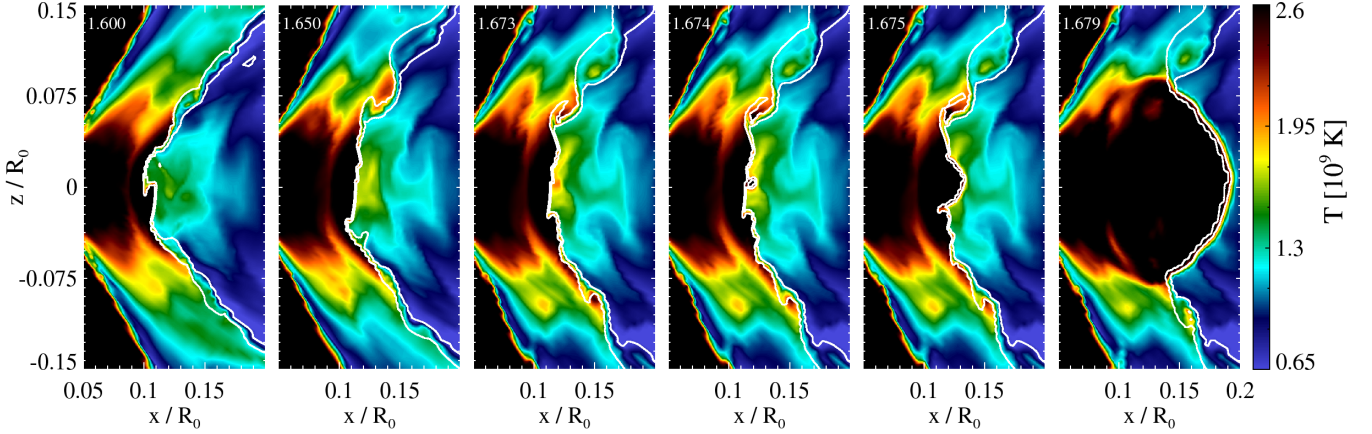
FIG. 3.— The effect of turbulence near the burning front on the onset of detonation in the model COq050_HR. Each panel shows snapshots of the temperature, with the time in units of the orbital time at $r = R_0$ displayed in the upper left corner. White contours correspond to fuel mass fractions $X_f = \{0.1, 0.4\}$. From left to right, the panels show: quasi-steady-state burning front ($t/t_{orb} = 1.600$), formation of an eddy by turbulence ($t/t_{orb} = 1.650$), hot spot prior to burning ($t/t_{orb} = 1.673$), hot spot after burning ($t/t_{orb} = 1.764$), and propagation of detonation ($t/t_{orb} = 1.675$ and 1.679). An animated version of this figure is available in the online version of the article.
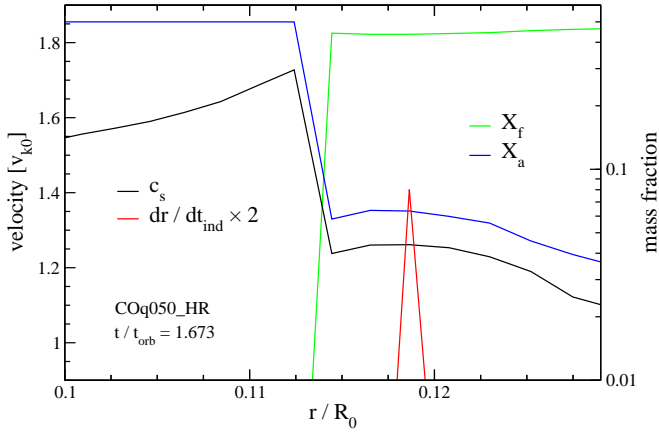
FIG. 4.— Radial profile of quantities angle-averaged over the hot spot that triggers a detonation at time $t = 1.673 t_{orb}$ in the model COq050_HR (Figure 3). Shown are the mass fraction of fuel (green), ash (blue), the sound speed (black), and the inverse of the induction time gradient (red). Mixing of ash upstream of the front is responsible for the increased temperature. This heating results in the condition $dr/dt_{ind} \sim c_s$ for spontaneous detonation (Appendix C) being approximately satisfied across the hot spot. The induction time is defined here as $t_{ind} = e_{int}/[\beta \dot{Q}_{nuc}]$, where $\beta = 29$ is the temperature exponent of the reaction rate (eq. [18]).

to increase with Ψ (§4.3, Fig. 7).

4.2. Detonations

We begin by elaborating on the evolution of torii which undergo detonation, basing our discussion on the high-resolution model COq050_HR (Figure 1). The angle-averaged thermodynamic quantities in the disk as a function of radius are shown in Figure 2 at different times. Also shown are various timescales in the disk as a function of radius, calculated at a time $t = 1.673 t_{orb}$, corresponding to the onset of the final detonation.

Because the sound crossing time is everywhere shorter than the viscous heating time, pressure equilibrium rapidly establishes a temperature profile that is nearly virial ($T \propto r^{-1}$) in regions of the disk where neutrino cooling is negligible. This profile becomes shallower than r^{-1} interior to the burning radius, because neutrino cooling becomes important and offsets viscous heating. The density also obeys a power-law radial

profile (for $\rho > \rho_0$; eq. [36]), with a slope that decreases with time as matter flows inwards. Such a profile steeping is expected since (at least in regular RIAFs) one expects $\rho \propto r^{-1/2}$ once steady-state accretion is reached on a timescale $t \sim t_{visc}$.

The inner edge of the torus ignites first, starting interior to the burning radius r_{nuc} predicted by equation (39). Burning requires a significantly higher temperature (and hence smaller radii) than at later times because initially the density is lower than ρ_0 (eq. [36]), below which nuclear reactions are artificially suppressed. If neutrino cooling is not included in our calculations, then a global detonation is triggered at these very early times if the value of Ψ is sufficiently high (model COq100_nc). Given that neutrino cooling is physically motivated and that detonations via the Zel'dovich mechanism may be suppressed if the effects of radiation pressure were properly included (Appendix C), we believe that such prompt detonations are unphysical, at least within the parameter regime of this study.[9] Verifying this will require simulations using a more detailed model of the initial structure of the disk and a more physical EOS.

When neutrino cooling is included or if Ψ is lower, then a prompt detonation is avoided and a steady-state burning front develops. The front settles at the expected radius $r \approx r_{nuc}$ within a few local dynamical times. A detonation can still be triggered at later times as the result of turbulence generated by fluid instabilities if Ψ is sufficiently high. The RT instability is somewhat suppressed by neutrino cooling when the value of Ψ is sufficiently large. At low Ψ, or in the absence of cooling, the burning front is noticeably distorted. Turbulence should be a ubiquitous feature of a more realistic MHD model since it can be generated directly by the MRI, rather than originating second-hand from convective instabilities.

Figure 3 shows a few snapshots of the region localized around the burning front in model COq050_HR, illustrating how turbulence triggers a detonation. Between 1.65 and 1.673 orbits, a turbulent eddy near the disk midplane mixes some of the hot downstream ash with the 'cold' upstream fuel, creating a hot spot just upstream of the burning front. If mixing

---

[9] During the tidal disruption of a more massive O-Ne WD, nuclear burning may begin during the circularization process itself. A dynamical detonation appears more likely to occur in this case.
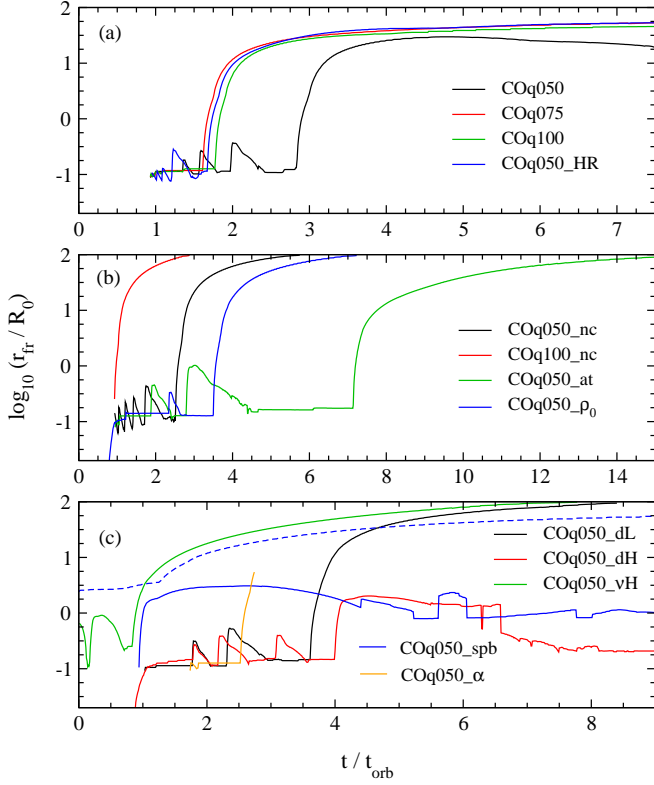
FIG. 5.— Radius of the outer edge of the burning front at the disk equator r_{fr} as a function of time, shown for several models that undergo explosions. The radius is calculated by searching for the outermost point where the ash mass fraction is equal to 0.25. Panel (a) shows models with high atmospheric density, while panels (b) and (c) show models that vary different parameters around the marginal model with low atmospheric density and neutrino cooling COq050_at. Note that the sawtooth shape of some curves signals multiple failed detonations in cases where Ψ is close to the critical value $\Psi_{crit} \simeq 1$ required for a successful large-scale detonation. The burning radius is $r_{nuc} \sim 0.1 R_0$ for the models shown (Table 3). The dashed curve in model COq050_spb in panel (c) denotes the outer edge of the torus; in this model the leading shock decouples from the burning front and stalls at $r \sim 50 R_0$.

FIG. 6.— Ratio of the mass in the torus M_{tor} to the initial WD mass as a function of time, for models that explode (Figure 5). The torus is defined as including all material with density $\rho \geq 10^{-3} \rho_{max}$. Non-exploding torii are not shown, as the decrease in mass is negligible on the same vertical scale. After explosion, the ash torus resumes accreting onto the central compact object, but at a reduced rate compared to disks which do not detonate (see Figure 7).

of ash and fuel is such that that the inverse gradient in the induction timescale $|\nabla t_{ind}|^{-1}$ across the eddy exceeds the local sound speed, then a localized burning front can transition into a detonation via the so-called Zel'dovich gradient mechanism (Zel'dovich et al. 1970; see Appendix C). We believe this provides a reasonable explanation for the delayed detonations observed in our simulations.

Figure 4 shows the mass fractions of fuel and ash across the hot spot, confirming that mixing is indeed involved in raising the fuel temperature. Also shown are the sound speed and the inverse of the induction time gradient across the eddy. The latter peaks at the hot spot at a value within a factor of ~ 2 of the sound speed, roughly consistent with the Zel'dovich threshold for a spontaneous detonation.

We now discuss the fate of detonations when parameters of the system are varied. The discussion is centered on variations in Ψ (eq. [37]), as it directly probes the dynamical effect of nuclear reactions on the disk. For each model, the value of this parameter shown in Table 3 is measured by first finding r_{nuc} just before explosion, and then computing the ratio of ε_{nuc} to the angle-averaged and mass-weigthed enthalpy at $r = r_{nuc}$. For non-exploding models, a time average value is taken. From equations (38) and (39) one can see that the (time-dependent) radial dependence of the temperature and density on radius have the most influence on the time varia-
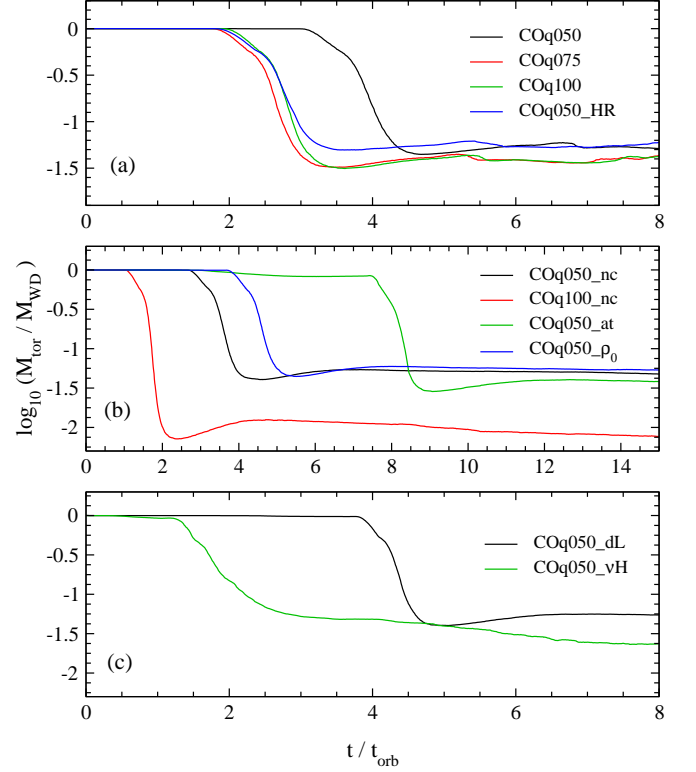
tion of Ψ in a given model. Nonetheless, the values obtained are generally close to what can be inferred from the initial properties of the disk.

Depending on the magnitude of Ψ relative to Ψ_{crit}, the hot spots generated by turbulence can produce three different outcomes. For $\Psi < \Psi_{crit}$, detonations remain localized and die out after propagating a distance comparable to the local radius. Multiple such *microexplosions* occur as the density of the inner accretion flow increases with time (Fig. 3). Although some of these temporarily enhance the thickness of the disk, accretion continues relatively steadily and the burning front remains stationary at $r \approx r_{nuc}$.

When Ψ is in the vicinity of Ψ_{crit}, hot spots can trigger large scale detonations, but many of them die out as they propagate outwards through the disk. Because burning occurs at a radius r_{nuc} interior to where the density of the torus peaks ($r \sim R_0$), such detonations are required to propagate against the density gradient. The weakening of the shock leads to a decrease in the resulting overpressure, decreasing the burning time behind the shock and hence the energy released over the region where the phase velocity of burning is supersonic. For slow enough burning, the shock degenerates into a pressure wave and damps (Niemeyer & Woosley 1997). Models with $\Psi \sim \Psi_{crit}$ are thus marginal in that they experience multiple failed detonations before a final explosion. Success is enabled in some cases by the changing radial density gradient, which decreases as the inner torus viscously evolves (Fig. 2). Since the probability of a successful detonation increases with time, one must follow the evolution for a sufficiently long time before establishing whether a marginal model will ultimately

TABLE 3
SUMMARY OF RESULTS

Model	$r_{\rm nuc}$[a] (R_0)	Ψ[b]	$t_{\rm exp}$[c] $(t_{\rm orb})$	$v_{\rm exp}$[d] (v_{k0})	$M_{\rm rem}$[e] $(M_{\rm WD})$	$t_{\rm ave}$[f] $(t_{\rm orb})$	$\langle\dot{M}_{\rm in}\rangle$[g] $(M_{\rm WD}/t_{\rm orb})$	$\langle\dot{M}_{\rm out}\rangle$[h]	$\langle X_{\rm a,out}\rangle$[i]	$\langle\dot{M}_{\rm unb}\rangle$[j] $(M_{\rm WD}/t_{\rm orb})$	Notes[k]
COq000	⋯	0.00	⋯	⋯	⋯	15-20	$10^{-2.6}$	$10^{-2.2}$	0	$10^{-4.3}$	q
COq010	0.26	0.14	⋯	⋯	⋯	15-20	$10^{-2.7}$	$10^{-2.1}$	$10^{-1.6}$	$10^{-4.2}$	q
COq025	0.21	0.31	⋯	⋯	⋯	15-20	$10^{-3.1}$	$10^{-1.9}$	0.2	$10^{-3.8}$	q
COq050	0.12	0.60	2.83	⋯	$10^{-1.2}$	8-10	$10^{-3.7}$	⋯	⋯	⋯	d,m,s
COq075	0.12	0.89	1.61	⋯	$10^{-1.4}$	8-10	$10^{-3.8}$	⋯	⋯	⋯	d,s
COq100	0.13	1.20	1.77	⋯	$10^{-1.4}$	8-10	$10^{-3.8}$	⋯	⋯	⋯	d,s
COq000_nc	⋯	0.00	⋯	⋯	⋯	11-16	$10^{-2.9}$	$10^{-2.1}$	0	$10^{-4.5}$	q
COq010_nc	0.23	0.13	⋯	⋯	⋯	11-16	$10^{-3.1}$	$10^{-2.1}$	0.1	$10^{-4.5}$	q
COq025_nc	0.18	0.28	⋯	⋯	⋯	11-16	$10^{-3.9}$	$10^{-2.0}$	0.2	$10^{-4.0}$	q
COq050_nc	0.10	0.48	2.51	2	$10^{-1.3}$	11-16	$10^{-4.3}$	⋯	⋯	⋯	d,m
COq100_nc	⋯	⋯	0.93	5	$10^{-2.1}$	11-16	$10^{-5.1}$	⋯	⋯	⋯	p
COq050_HR	0.11	0.60	1.67	⋯	$10^{-1.2}$	8-10	$10^{-3.7}$	⋯	⋯	⋯	d,m
COq050_at	0.17	0.60	7.13	1	$10^{-1.4}$	11-16	$10^{-3.7}$	⋯	⋯	⋯	d,m
COq050_ρ_0	0.13	0.55	3.49	2	$10^{-1.3}$	11-16	$10^{-3.6}$	⋯	⋯	⋯	d,m
COq050_dL	0.15	0.64	3.61	1	$10^{-1.3}$	8-13	$10^{-3.6}$	⋯	⋯	⋯	d,m
COq050_dH	0.15	0.70	⋯	⋯	0.7	12-17	$10^{-4.9}$	$10^{-1.5}$	$10^{-1.6}$	$10^{-2.8}$	q,m
COq050_νH	0.25	0.63	0.83	1	$10^{-1.6}$	6-8	$10^{-2.9}$	⋯	⋯	⋯	d,m
COq050_spb	⋯	⋯	0.94	⋯	0.19	8-10	$10^{-4.6}$	⋯	⋯	⋯	p,s
COq050_ss	0.13	0.63	2.52	⋯	⋯	⋯	⋯	⋯	⋯	⋯	d,m
CO_f1	0.21	0.91	⋯	⋯	0.87	11-16	$10^{-4.2}$	$10^{-1.8}$	0.3	$10^{-2.0}$	q
CO_f2	0.11	1.00	0.56	1	$10^{-1.9}$	9-11	$10^{-3.4}$	⋯	⋯	⋯	d
HE_00	⋯	⋯	⋯	⋯	⋯	1-3	$10^{-2.2}$	$10^{-0.9}$	⋯	$10^{-1.7}$	q
HE_f1	0.024	0.32	⋯	⋯	⋯	1-3	$10^{-2.3}$	$10^{-0.9}$	$10^{-2.2}$	$10^{-1.6}$	q

[a] Radius of the steady-state burning front. For delayed explosions, measured just before the last detonation sets in; time-averaged value for quiescent models. Not measured in prompt explosions.

[b] Ratio of $\varepsilon_{\rm nuc}$ to the enthalpy (angle-averaged and mass-weighted) at the burning radius (eq. [37]), right before explosion or time-averaged if non-exploding.

[c] Time of the final detonation (exploding models only).

[d] Expansion velocity at the time when shock reaches the domain boundary ($100R_0$), in units of $(GM_c/R_0)^{1/2}$ (exploding models with low ρ_∞ only).

[e] Mass of the remnant torus (only applicable to exploding models).

[f] Time range for average properties (quiescent models) or remnant mass (exploding models) calculation.

[g] Time-averaged net accretion rate through the inner boundary.

[h] Time-averaged net mass-loss rate at $r = 4R_0$.

[i] Ratio of net time-averaged mass-loss in nuclear ash to total ejecta, evaluated at $r = 4R_0$.

[j] Time-averaged mass-loss rate at $r = 4R_0$, including unbound material only.

[k] Outcomes: quiescent accretion (q), delayed explosion (d), multiple detonations before explosion (m), prompt explosion (p), ejecta stalls (s).

succeed or fail to explode.

For large $\Psi \gg \Psi_{\rm crit}$, the energy released by even the first detonation is sufficient to pass the point of maximum density. Our parametric sequence of simulations indicate that this critical value $\Psi_{\rm crit} \approx 1$ appears to be relatively insensitive to whether neutrino cooling is included or not. The final column of Table 3 summarizes the outcome of each simulation.

Figure 5 shows the time evolution of the burning front radius $r_{\rm fr}$ at the disk midplane in several models which ultimately result in explosions. When Ψ is large (such as in COq100), then the burning front remains near $r_{\rm nuc}$ until the first detonation occurs. The sawtooth shape of the burning front evolution for 'marginal' models (such as COq050) signals multiple failed detonations before the final successful explosion. The top and middle panels of Figure 5 compare $r_{\rm fr}(t)$ in models with and without neutrino cooling. Changing the resolution does not alter the qualitative outcome as inferred from comparing models COq050 and COq050_HR. The higher resolution model explodes earlier while still undergoing multiple detonations.

Variations around the marginal model with low atmospheric density (COq050_at) show that a lower thermal content and faster accretion are more conducive to detonations. Models COq050_dL and COq050_νH both explode earlier than the marginal model. A lower cutoff density ρ_0 also causes the disk to explode earlier. Note however that the value of Ψ is remarkably close to 0.6 for all the exploding models that use the power-law burning rate. In contrast, model COq050_dH does not undergo a global detonation. Counterintuitively, this model has a higher temperature normalization, but the detonation fails to sweep through the whole disk. We surmise that the larger extent of the disk plays a role in this failure.

The functional form of the viscous stress does not appear to greatly influence the outcome, so long as the strength is comparable. Models COq050_α and COq050_spb probe the effects of using the viscosity prescriptions in equations (14) and (15). The amplitude is chosen so that the inner edge of the torus reaches the inner boundary at around the same time as in model COq050_at. Whereas model COq050_α undergoes a vigorous explosion (so much so that the model crashes after 3 orbits), model COq050_spb instead develops a prompt explosion that fizzles because the leading shock and the burn-
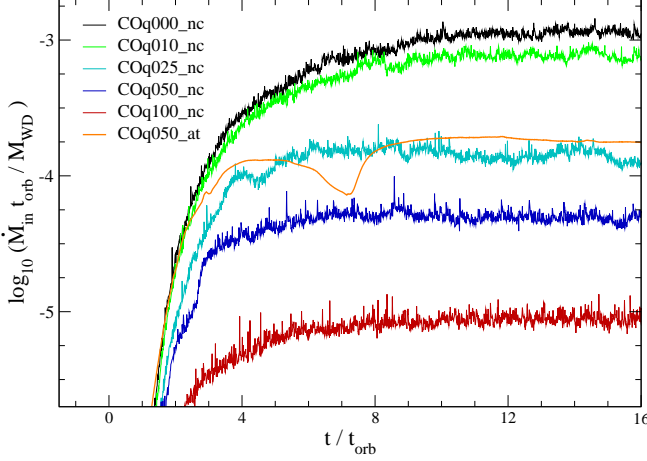
FIG. 7.— Mass accretion rate $\dot{M}_{in}$ at the inner boundary ($r_{in} = 0.01R_0$) as a function of time, shown for models with low atmospheric density. All models shown (except for COq050_at) neglect neutrino cooling. Note that as Q [Ψ] is increased from 0 to Q_0 [1.8], the peak accretion rate decreases by over two orders of magnitude. The decrease in $\dot{M}_{in}$ arises either as the result of a large-scale detonation (when $\Psi > \Psi_{crit}$) or due to enhanced convection and polar outflows (when $\Psi < \Psi_{crit}$; see Fig. 8).

FIG. 8.— *Top:* Comparison of time-averaged mass fluxes as a function of radius in non-exploding models COq000_nc (no burning, black curves) and COq025_nc ($Q/Q_0 = 0.25$, cyan curves). Outflow, inflow, and net fluxes are shown as dot-dashed, dashed, and solid curves, respectively. The vertical dotted line corresponds to the time-averaged burning radius r_{nuc}. *Bottom:* Root-mean-square Mach number as a function of radius in the disk midplane for the same set of models. The energy deposition from nuclear burning causes a localized increase in the turbulent kinetic energy, decreasing the net mass flux through the disk inside r_{nuc} (compare with Figure 7).

ing front decouple from one another.

Models CO_f1 and CO_f2 employ the full functional form of the $^{12}C(^{12}C,\gamma)^{24}Mg$ reaction, and assume the full energy release ($Q = Q_0$). They differ in their thermal content and strength of the viscosity. The model with higher thermal content and lower viscosity does not explode (CO_f1), whereas the other (CO_f2) does undergo a large scale detonation. Because a reasonable variation in the model parameters results in a qualitative change in the predicted outcome, this implies that the true evolution is sensitive to the details of the accretion physics. Determining whether disk detonation is indeed a robust outcome of C-O WD-NS mergers in Nature will thus require simulations which include both a more physical EOS and account for other details, such as the true MHD nature of the disk turbulence.

Finally, we find that the He disk model with the triple-alpha reaction (HE_f1) fails to detonate, in part because the burning begins at a radius where Ψ is small. Also, the weaker temperature dependence of the reaction rate leads to a burning front that is more spread out in radius than in the C-O WD case, leading to a more spatially distributed energy release. This situation may be less conducive to detonations generated by mixing across a well-defined burning front.

Table 3 gives the time of the final detonation for each exploding model and the shock velocity once it reaches the outer simulation boundary at $r = 100R_0$. In models with low atmospheric density ($\rho_\infty = 10^{-7.7}\rho_{max}$) the velocity asymptotes to a nearly constant value of order of the Keplerian speed near the radius of the original torus $v_{k0} = (GM_c/R_0)^{1/2}$ (~ 3000 km s^{-1} in our fiducial C-O WD models). By contrast, in models with high background density ($\rho_\infty = 10^{-5.7}\rho_{max}$) the velocity decreases and the radius of the burning front comes to an effective halt. This outcome is an artifact of the high inertia of the atmosphere, as is clear by comparing the evolution of models COq050 and COq050_at, which differ only in the value of ρ_∞. In order to accurately predict the asymptotic properties of outflows from the disk, and hence their resulting observational signatures, one must use a sufficiently low atmospheric density for which the shock motion is converged. We have not undertaken such a convergence study here, since our pri-
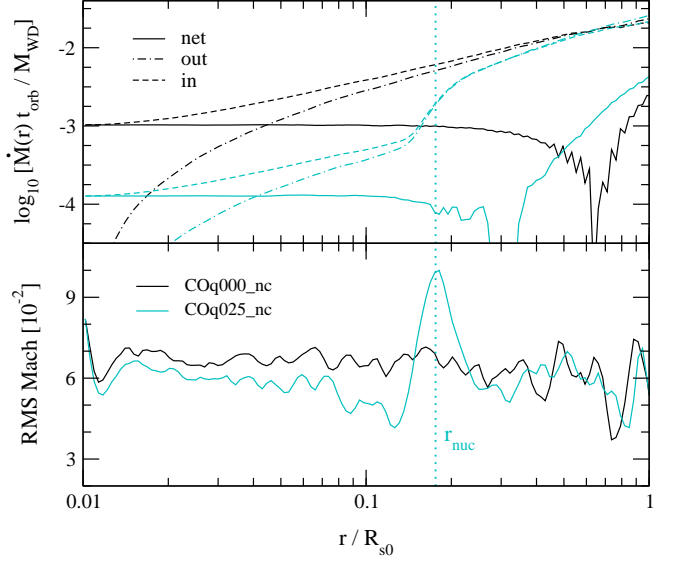
mary goal is understanding the basic dynamics of the disk on smaller scales. Also note that the density suppression of the burning rate (eq. [36]) ensures that no burning takes place after the detonation has swept the initial torus material.

Disks that explode leave behind a remnant torus composed primarily of ash. Figure 6 shows the time evolution of the torus mass M_{tor}, defined as that enclosed within the density contour $\rho \geq 10^{-3}\rho_{max}$, in several disk models. The remnant disk after explosion contains between 1% and 10% of the initial WD mass, depending on the value of Ψ and on whether neutrino cooling is included. The existence of such a disk implies that the accretion rate onto the central compact object does not immediately fall to zero in disks that explode (see also Figure 7).

4.3. *Quiescent Disks and Explosion Remnants*

Although small-scale runaway burning and localized microexplosions may occur for $\Psi < \Psi_{crit}$, the disk as a whole never detonates. The properties of disks with nuclear heating are nevertheless qualitatively different from those without burning. In this section we discuss these NuDAFs which undergo quiescent accretion.

Figure 7 shows the time evolution of the net mass accretion rate at the inner boundary $\dot{M}_{in}$ for the sequence of C-O torii without neutrino cooling, for various values Ψ. This sequence was chosen since its low atmospheric density ρ_∞ allows us to better study the properties of disk outflows. The asymptotic accretion rate monotonically decreases with increasing Ψ, with $\dot{M}_{in}$ dropping by more than two orders of magnitude as Ψ increases from 0 to ~ 1. For large values of $\Psi > \Psi_{crit}$, this decrease in the accretion rate is the result of the mass loss caused by the disk detonation, which leaves only a small remnant torus (Fig. 6). However, even for disks that do not explode, the mass accretion rate is substantially reduced by the effects of nuclear heating (e.g., model COq025_nc).
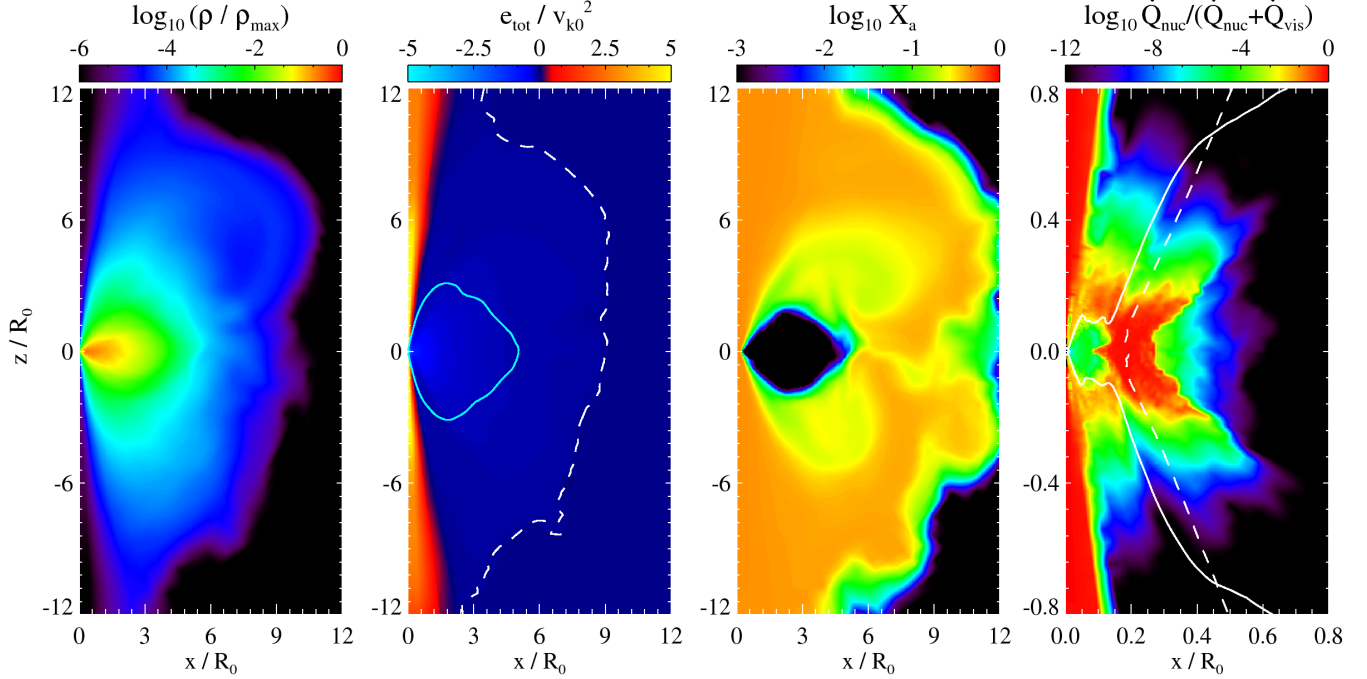
FIG. 9.— Time-averaged properties of the quiescently accreting NuDAF model COq025_nc, averaged between orbits 11 and 16. Quantities displayed (from left to right) include the density ρ; total energy e_{tot} (thermal + kinetic - gravitational); mass fraction of ash X_a; and fraction of the total heating $\dot{Q}_{tot} = \dot{Q}_{nuc} + \dot{Q}_{vis}$ contributed by nuclear heating. The light blue contour in the energy panel corresponds to $\rho/\rho_{max} = 10^{-3}$, marking the approximate surface of the torus. The dashed white contour shows the region where the mass fraction of atmospheric material is more than 0.1% by mass (the atmosphere is very unbound by construction; we set its energy to zero in this plot to maximize contrast between regions dominated by torus material). The solid white contour on the heating ratio panel corresponds to $\dot{Q}_{visc} = 10^{-4} v_{k0}^3/R_0$, while the dashed contour denotes the burning front ($X_a = 0.25$). Note that both heating terms are suppressed for $\rho < 10^{-3} \rho_{max}$ (eq. [36]), hence there is negligible heating inside the polar funnel. Also note the different spatial scale of the rightmost panel.
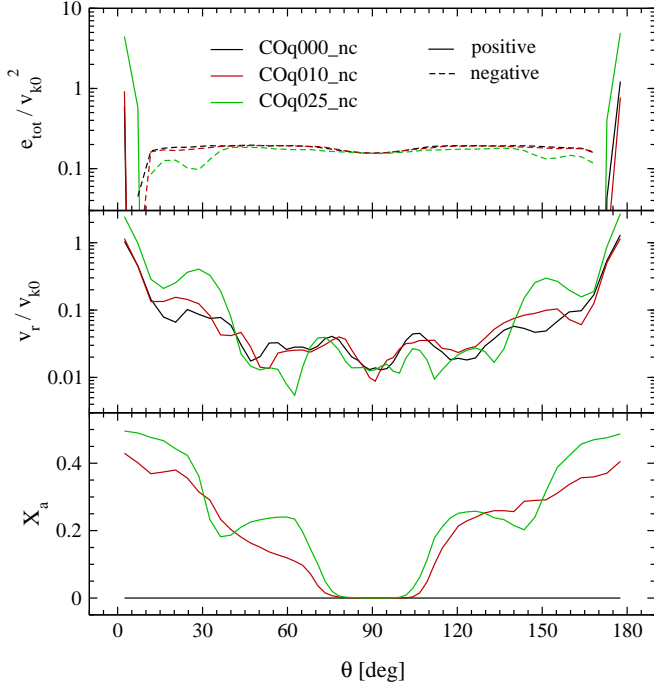
FIG. 10.— Time-averaged quantities at $r = 4R_0$ as a function of polar angle, for three quiescent models that differ in the strength of nuclear burning. Shown are (a) the total energy, (b) radial velocity, and (c) mass fraction of nuclear ash.

The decrease in the net accretion rate in quiescent NuDAFs results from more vigorous convection, driven by the en-

hanced heating from nuclear reactions. This is illustrated in Figure 8, which shows the time- and angle-averaged mass fluxes as a function of radius for models with and without nuclear burning. A localized enhancement in the turbulent kinetic energy (as measured by the root-mean-square Mach number) around the time-averaged burning radius coincides with a sharp drop in the mass fluxes in model COq25_nc.

For comparison, Figure 7 also includes a low-ρ_∞ model *with* neutrino cooling included (COq050_at). The net accretion rate for this model is a smoother function of time than the otherwise identical model without cooling (COq050_nc), due to the near cancellation of viscous heating by neutrino cooling (c.f. Figure 2, bottom panel), which suppresses convection. This is also responsible for the larger magnitude of the net mass flux.

In order to better understand the properties of disk outflows from quiescent NuDAFs, we perform time-averages of the flow over several orbits once they have reached a quasi-steady state (c.f. Stone et al. 1999). Figure 9 shows two-dimensional maps of density, total energy, ash mass fraction, and heating strength for model COq025_nc, averaged between orbits 11 and 16. Material is unbound when its total energy

$$e_{tot} = \frac{1}{2}\left[v_r^2 + v_\theta^2 + \frac{\ell_z^2}{(r\sin\theta)^2}\right] + e_{int} - \frac{GM_c}{r}, \qquad (40)$$

is positive. Figure 9 shows that disk material satisfying this condition is confined to within a narrow funnel $\sim 10°$ from the polar axis. This unbound flow is composed primarily of nuclear ash and inert species. The distribution of nuclear ash is wider than this funnel, however. Figure 9 also shows that a significant fraction of the outflowing ash is bound, circulat-
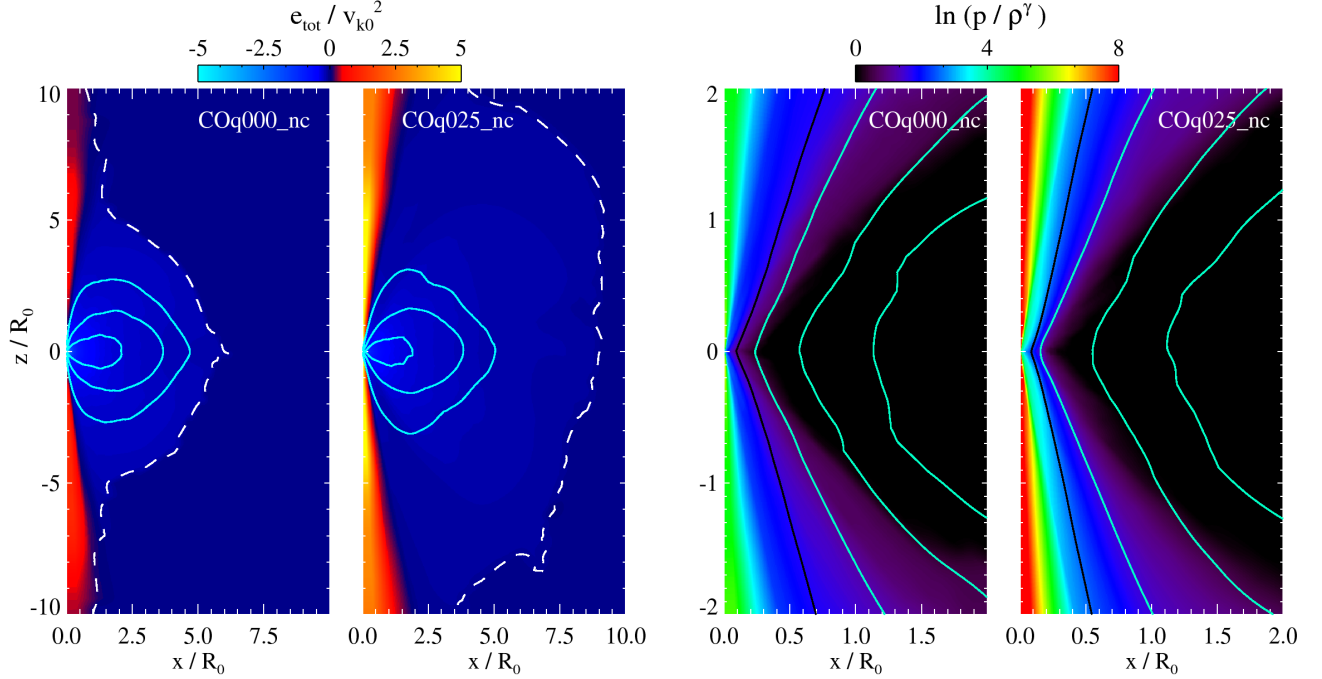
FIG. 11.— Comparison of time-averaged properties between a model with nuclear burning (COq025_nc) and one without (COq000_nc). The average is taken between orbits 11 and 16. The left two panels show the total energy, with solid contours corresponding to densities $\rho/\rho_{max} = \{10^{-3}, 10^{-2}, 10^{-1}\}$. White dashed contours mark the surface where the atmosphere is 0.1% of the fluid by mass (outside of which we plot the total energy as zero, to maximize contrast). The right two panels show a function proportional to the entropy of the gas, zoomed in on the region surrounding the burning front. Contours correspond to angular momenta $\ell_z = \{0.25, 0.4, 0.65, 0.9\}(GM_cR_0)^{1/2}$. The higher entropy of the polar funnel in the case of nuclear burning indicates excess heating. This is seen in the difference between the time-average mass loss rate in unbound material, which is $\langle \dot{M}_{unb} \rangle = 10^{-6} M_\odot \ s^{-1}$ and $3 \times 10^{-7} M_\odot \ s^{-1}$ in the cases with and without nuclear heating, respectively.

ing above the disk and returning to the midplane at distances larger than the outer radius of the disk. The angular distribution of the total energy, radial velocity, and ash for the quiescent models with no neutrino cooling are shown in Figure 10. Note that the expansion velocity along the funnel can reach the Keplerian velocity v_{k0} at the circularization radius, which for the fiducial C-O WD-NS merger is ~ 3000 km s^{-1}.

The rightmost panel in Figure 9 shows the fraction of the total heating in the disk contributed by nuclear burning. Nuclear heating is important relative to viscous heating in a region centered around r_{nuc} on the disk midplane. Note that the time-averaged thickness of this region ($\sim r_{nuc}$) is larger than the instantaneous thickness of the burning region in the case of a detonation (Fig. 4).

Figure 11 compares the time-averaged disk properties of otherwise identical models with and without nuclear burning (COq025_nc and COq000_nc, respectively). The most significant effect of nuclear burning lies in the properties of the polar funnel, which is more unbound than in the model without nuclear burning. This difference also manifests in the entropy, which is higher inside the funnel for disks with burning. A higher entropy indicates excess heating in low temperature regions, as could result from additional heating above the midplane due to the enhanced convection from nuclear burning (Fig. 8). An entropy-increasing heating profile is precisely the kind necessary to power an energetic outflow, as is well known in other astrophysical contexts such as the solar wind.

Nuclear burning does not greatly affect the structure of the disk ($\rho > \rho_0$; eq. [36]), although regions with lower density are $\sim 50\%$ more extended in radius. The presence of nuclear

burning also does not alter the fact that surfaces of constant entropy and angular momentum are parallel, as is found in hydrodynamic simulations of RIAFs (e.g., Stone et al. 1999). This indicates that the disk is still marginally stable to convection, even when the energy input by nuclear heating is included.

Table 3 gives the time-averaged net accretion rate $\langle \dot{M}_{in} \rangle$ at the inner boundary, total outflow rate, as well as unbound outflow at $r = 4R_0$ in our quiescently-accreting models. Note that $\langle \dot{M}_{unb} \rangle$ increases with Ψ. In non-exploding models with parametric burning rate, the mass loss in unbound material approaches a substantial fraction of $\langle \dot{M}_{in} \rangle$ as $\Psi \to \Psi_{crit}$. The fraction of ash in the unbound outflow also correlates with Ψ.

The decrease of the mass accretion rate with Ψ allows the disk to survive for a time longer than the characteristic viscous time. Model CO_f1 is an extreme in this sense. The mass-loss in unbound flows exceeds the accretion rate by two orders of magnitude. Most of the WD material will be ejected over ~ 100 orbits, or about 1.5 hours as an unbound flow with a velocity ~ 1000 km s^{-1}. Converting to physical units, the mass loss rate in unbound material can lie in the range $10^{-5} - 10^{-3} \ M_\odot \ s^{-1}$ for the full range of models explored.

5. DISCUSSION

5.1. Implications for WD-NS/BH mergers

An obvious implication of our results is that the C-O torii created by WD-NS can undergo a large-scale detonation and explosion. This explosive evolution differs drastically from

the steady-state model for NuDAFs envisioned by M12,[10] although the M12 model does provides a qualitative description of the quiescent mode of accretion found to occur when $\Psi < \Psi_{crit}$. A similar conclusion would likely apply to the case of a hybrid He-C-O WD because the reaction ^{4}He$(^{16}$O$,\gamma)^{20}$Ne has a similar threshold Ψ_{crit} for detonation (Table 2). Given the ubiquity of turbulence generated by the MRI in physical accretion disks and relative ease with which the requisite conditions for a detonation are met (Appendix C), it is possible that detonation is a robust outcome of any disk with $\Psi \gtrsim 1$ under the influence of a sufficiently temperature-sensitive nuclear reaction. Our picture of turbulence-generated detonations in many ways resembles that invoked in 'pulsation delayed detonation' models for Type Ia SNe (e.g., Khokhlov et al. 1997; Niemeyer & Woosley 1997).[11]

Although detonations appear to be a common feature of disk evolution when $\Psi \gtrsim 1$, it is challenging to make a definitive statement about the ubiquity of a detonation because there are hints that the outcome could depend on more parameters than Ψ alone. For instance, our models CO_f1 and CO_f2 with full reaction rates included have relatively minor differences in their parameters, yet one explodes while the other does not. The precise composition of the WD may also matter since Ψ is proportional to the fuel mass fraction X_f.

Another important caveat is that our current EOS includes only ideal gas pressure, despite the fact that radiation pressure is important at small radii and early times in the disk evolution. Since radiation pressure acts to reduce the temperature at a given pressure, this implies that (1) a deeper potential well is required for burning, thus reducing the value of Ψ; and (2) the likelihood that runaway burning will occur is also reduced since the magnitude of temperature fluctuations across the burning front are suppressed (Appendix C). It is thus possible that radiation pressure could suppress a detonation at early times in the torus evolution. However, this should not be the case once steady-state accretion is achieved on a timescale $\sim t_{visc}$ since then the density of the inner accretion flow is sufficient for gas pressure to dominate. The radially-decreasing density profile achieved on a timescale $t \gtrsim t_{visc}$ is also the most conducive to a sustaining an outward-propagating detonation (§4.2). This gives us confidence that the threshold for detonation found in our simulations is not an artifact of our EOS.

One consequence of a relatively prompt detonation is that a large fraction of the WD is unbound, which substantially limits the mass ultimately accreted by the central NS. This makes it less likely that a black hole will be created following a WD-NS merger (Paschalidis et al. 2011). A prompt explosion also limits the energy of a relativistic outflow (i.e. a 'jet') originating from the vicinity of the compact object (King et al. 2007) and its resulting high energy or radio emission. Even when a strong detonation occurs, however, the existence of a remnant disk of bound material (Fig. 6) indicates that a small mass $\sim 10^{-2} M_\odot$ is still available to accrete.

---

[10] M12 did show that his solutions were prone to thermal instability due to the sensitive temperature dependence of nuclear reactions. Although one interpretation of our results is that such instabilities manifest as a detonation, the M12 model only accounts for the properties of the mean flow and not for the role of turbulence, which plays such an essential role in the detonation process in our simulations.

[11] How the deflagration ignited near the core of a Chandrasekhar-mass C-O WD transitions into a detonation remains a major theoretical uncertainty in standard Type Ia supernova models. Assuming that the initial deflagration fails to unbind the WD, delayed detonation models invoke a secondary detonation which results from the mixing of partially-burned fuel and ash following the subsequent contraction of the WD.

Our highly idealized initial conditions are necessarily different from torii that arise in self-consistent mergers. On the one hand, the disruption process is not instantaneous (e.g., Fryer et al. 1999), thus the angular momentum distribution will not be constant. Also, the thermalization of the rotational kinetic energy by shocks likely leads to a non-uniform entropy distribution in the disk. If detonations early in the accretion phase turn out to be a prevalent outcome, then the initial form of the torus will be an important factor to consider when making observational predictions. This would also imply that the angular momentum transport process must be treated correctly. However, we do not expect some of the more general results of this paper, such as the existence of a critical value of $\Psi \sim 1$ for detonation or the dependence of quiescent outflows on Ψ, to depend fundamentally on the details of the initial condition.

In the case of a WD-BH merger, the larger mass of the central compact object results in a lower value of $\Psi \propto M_c^{-1}$, making it more likely that accretion will instead occur in the quiescent regime ($\Psi < \Psi_{crit}$). If non-explosive burning allows a larger fraction of the WD to accrete, then the power of an associated high energy counterpart (Fryer et al. 1999) may be larger than in the WD-NS case. One limitation on the rate of such events is that a binary with a high mass ratio is required for unstable mass transfer to occur in the first place ($q \gtrsim 0.2 - 0.5$; Paschalidis et al. 2009). The low mass black holes ($M_c \lesssim 5 M_\odot$) thus required appear to be relatively rare among the population of Galactic binaries (e.g., Bailyn et al. 1998; Fryer et al. 2012).

In contrast to C-O torii, He torii appear unlikely to explode, even under conditions we find conducive to a detonation (Tables 1 and 3). Stability results mostly from the weaker temperature dependence of the triple$-\alpha$ nuclear reaction rate at high temperature, which makes the conditions for detonation via turbulent mixing less likely to be satisfied (Appendix C). The torus density in our simulation is sufficiently low that a large fraction of ^{4}He may reach sufficiently high temperature to photodissociate before burning into heavier elements. Our conclusion that He torii are unlikely to detonate is at odd with the suggestion of Schwab et al. (2012) that such detonations might occur in disks created by WD-WD mergers. One possible difference in their case could be the importance of degeneracy pressure or the higher densities achieved by compression due to the presence of a WD surface.

Another limitation of applying our current simulations directly to physical mergers is that we include only a single reaction. In some cases this could affect our conclusions about the likelihood of a detonation. Although pure helium torii appear to be stable, the products of He burning (^{12}C or ^{16}O) are themselves prone to explosive burning. In C-O torii, on the other hand, subsequent reactions (e.g., oxygen burning) will generally occur much deeper in the potential well (lower r_{nuc} and hence lower Ψ; Table 2), such that the first reaction has the largest dynamical impact. Nevertheless, including a full reaction network could result in a much richer evolutionary history, with, for instance, several potential detonations occuring in succession as matter slowly sinks deeper into the potential well and burns to increasing heavier elements. This behavior may qualitatively resemble the late stages of unstable shell burning in massive stars (e.g., Arnett & Meakin 2011; Quataert & Shiode 2012) or pulsational pair instability supernovae (e.g., Woosley et al. 2007).

5.2. *Supernova-Like Optical Transients*

M12 proposed that the ejecta from a WD-NS/BH merger could produce an optical transient, powered by the radioactive decay of ^{56}Ni synthesized in the accretion disk. He was motivated by the recent discovery of several Type I supernovae which are dimmer and/or more rapidly evolving than normal SNe Ia or Ib/c (e.g., Li et al. 2003; Jha et al. 2006; Foley et al. 2009; Perets et al. 2010; Waldman et al. 2011; Kasliwal et al. 2011). The rapid evolution and low luminosities of these events require both lower ^{56}Ni yield and lower total ejecta mass than values characteristic of normal SNe. Some of these events occur in locations far outside of their host galaxies (Perets et al. 2010; Kasliwal et al. 2011), possibly consistent with the location of a WD-NS merger if the NS was given a natal 'kick'.

Based on a steady-state model of accretion following a WD/NS-BH merger, M12 predicted an ejecta composed primarily of unburned C-O or He (depending on the initial WD) along with a range of intermediate mass elements and a small quantity of ^{56}Ni. Since our calculations in this paper include only a single reaction, we cannot directly predict the Ni yield or precisely determine the velocity structure of the ejecta. Nevertheless, we can address whether qualitative features of the outflows are consistent with those required to produce a supernova-like transient.

In the case of quiescent disk evolution (§4.3), the picture that we find is qualitatively similar to that of M12. Nuclear reactions power a quasi-steady outflow with an enhanced mass-loss rate over the case without nuclear burning (Fig. 11). If $\Psi < \Psi_{\rm crit}$ is satisfied for the first reaction activated at large radii in the disk, then this condition will also be satisfied for subsequent reactions which release at most a comparable amount of energy but occur deeper within the potential well. The total mass of ^{56}Ni ejected is indeed likely to be small $M_{\rm Ni} \sim 10^{-3} - 10^{-2} M_\odot$, because mass loss from the outer disk cuts off the supply reaching smaller radii where the ^{56}Ni produced. Note, however, that since our simulations show that unbound outflows from the disk primarily originate from regions interior to the burning radius (Figs. 9, 10), this suggests that the M12 model may overestimate the fraction of unburned fuel in the ejecta.

On the other hand, if the disk undergoes a global detonation (§4.2), then this picture is drastically altered. In this case the yield of intermediate mass elements and ^{56}Ni will instead depend on how far nuclear reactions proceed behind the detonation front. Since the average density of the outer disk is relatively low compared to that of the original WD, the mass of ^{56}Ni synthesized will almost certainly be much less than in a normal Type Ia SNe (cf. Sim et al. 2010). How much Ni is produced will depend on the time of detonation $t_{\rm det}$ relative to the viscous time of the torus $t_{\rm visc}$ (eq. [8]). If $t_{\rm det} \ll t_{\rm visc}$, then only a small fraction of the torus mass has spread to small radii where the density is sufficiently high for ^{56}Ni to be produced, while if $t_{\rm det} \sim t_{\rm visc}$ then an larger fraction of the shocked WD material will be processed to ^{56}Ni. Our current simulations show that the former case ($t_{\rm det} \ll t_{\rm visc}$) is more likely, but it is still possible that the latter case is more physical if radiation pressure indeed suppresses early detonations.

5.2.1. *Connection to SN 2002cx-like Events?*

One type of SNe with characteristics seemingly compatible with those resulting from a WD-NS/BH merger are the events

prototyped by SN 2002cx and SN 2005bj ("SN 2002cx-like" events; Li et al. 2003; Jha et al. 2006; Phillips et al. 2007; Foley et al. 2009). This rare class of Ia SNe are in part distinguished by the following features: (1) high ionization spectrum at maximum light, and the presence of elements lighter than the Fe group at all epochs, both indicating that the ejecta is extensively mixed; (2) a low peak luminosity compared to that expected given its rate of decline (i.e. not following the standard 'Phillips relation'), indicating a wide range of synthesized ^{56}Ni mass, ranging from $M_{\rm Ni} \sim 3 \times 10^{-3} - 0.2 M_\odot$; (3) low expansion velocities $\sim 3000 - 5000$ km s^{-1} (hence low kinetic energy) compared to a normal SN Ia ($\sim 10,000$ km s^{-1}); (4) permitted Fe II lines and continuum photospheric emission at late times, indicating very low velocities $\lesssim 1,000$ km s^{-1} for the innermost ejecta; and (5) host galaxies with both active star formation (Foley et al. 2009) as well as older stellar populations (Foley et al. 2010). (6) An estimated occurence rate $\lesssim 10\%$ of that of normal SNe Ia (e.g. Phillips et al. 2007).

Many of the above characteristics are qualitatively consistent with the expected SN produced by a disk detonation following a WD-NS or WD-BH merger. Given that a wide range in disk densities is expected depending on the mass ratio of the binary, one likewise expects a wide range in the mass of ^{56}Ni and intermediate mass elements. Extensive mixing also seems plausible given the asymmetric nature of the explosion. Low velocity of the inner ejecta is also predicted, since the inner ejecta is substantially slowed by the gravitational field of the central compact object (not present in a usual Type Ia event). Although the expected population of host galaxies is difficult to predict with confidence, a mixture of both early and late-type galaxies is likely (e.g. Belczynski et al. 2002), given the distribution of gravitational wave inspiral times. The lack of spectroscopic evidence for unburned ^{12}C in SN 2002cx-like events is also compatible with a disk detonation model, though this observation is in tension with alternative models invoking the pure deflagration of a Chandrasekhar-mass WD (e.g., Blinnikov et al. 2006). The rate of WD-NS mergers in the Milky Way is also estimated to be $\sim 10^{-4}$ yr^{-1} (based on known population of tight WD-NS binaries; O'Shaughnessy & Kim 2010), or approximately $\sim 3\%$ of the SN Ia rate. One potential problem with the disk detonation model is the continuum polarization, which one would naively expect to be high given the large asymmetry, yet at least in one case (2005hk) was observed to be small ($\sim 0.4\%$; Chornock et al. 2006).

We will explore the properties of supernovae from WD-NS/BH mergers in greater detail in future work using the properties of outflows from the torus including a full α-reaction network. These will allow us to better test whether WD-NS/BH mergers can be associated with 2002cx-like events or other classes of subluminous Type I SNe.

5.3. *Implications for Collapsar Accretion Disks*

Another application of our results is to accretion disks formed by the collapse of rotating stars, as in collapsar models for gamma-ray bursts (GRBs) (MacFadyen & Woosley 1999; Lindner et al. 2012). Depending on the angular momentum profile of the star (Woosley & Heger 2006), a significant fraction of the collapsing envelope may circularize at sufficiently large radii $\gtrsim$ few $\times 10^8$ cm, where nuclear reactions such as ^{4}He(^{16}O,γ)^{20}Ne are important. Given the relatively low mass of the black hole formed by the collapse of a Wolf-Rayet star, one expects $\Psi \sim \Psi_{\rm crit}$ in collapsar disks, such that nuclear

burning could indeed impact the dynamics of the accretion flow. If the effects of nuclear burning produce large amplitude fluctuations in the central accretion rate, then the viscous or dynamical timescale near the burning radius ($\sim$ seconds for $r_{\rm nuc} \sim$ few $\times 10^8$ cm) could be imprinted on the variability of GRB emission. This could explain, for instance, why the power density spectra of GRB light curves peaks at a frequency $\sim$ Hz (Beloborodov et al. 2000) which is much lower than the $\sim$ kHz variability characteristic of the innermost stable orbit.

Quiescent outflows, or periodic episodes of runaway burning, could also provide a source of ^{56}Ni, as is required to power the light curves of GRB supernovae. Bodenheimer & Woosley (1983) first showed that a sufficiently rapidly rotating star could undergo explosive oxygen burning upon collapse, due to heating caused by the centrifugal 'hang up' of infalling material (cf. MacFadyen & Woosley 1999). How much ^{56}Ni is synthesized from such explosive burning of stellar fuel, versus that produced within much hotter outflows from the inner torus (MacFadyen & Woosley 1999; Metzger et al. 2008; Milosavljević et al. 2012; Surman et al. 2011), has yet to be quantified.

Nuclear burning may equally be important in accretion following the merger of a He star with a NS or BH (Fryer & Woosley 1998). Thöne et al. (2011) proposed that a He star-NS merger was responsible for the highly unusual "Christmas" gamma-ray burst 101225A, which exhibited exceptionally long gamma-ray and thermal X-ray emission. In order to explain the peak luminosity of the optical 'bump' following this event as supernova-like emission, the ejected mass of ^{56}Ni must have been small $\lesssim 0.1 M_\odot$ (if one adopts the distance advocated by Thöne et al. 2011). Future work on NuDAFs will better address the accretion efficiency and ^{56}Ni ejected due to rapid He accretion, thereby allowing us to assess whether the high energy and thermal optical emission from GRB 101225A was indeed compatible with a He star-NS merger.

6. SUMMARY

This paper explores the effect of nuclear reactions on the evolution of RIAFs, in the context of merging WDs and NSs or BHs. Two-dimensional hydrodynamic simulations with FLASH3.2 are used to systematically characterize the properties of these disks. Our main findings are the following:

1. – The effect of nuclear burning on RIAFs is controlled by the ratio Ψ of the nuclear energy to the enthalpy at the radius $r_{\rm nuc}$ where most of the fuel is consumed (eqns. [37] and [39]). The qualitative behavior of the system depends on the value of Ψ relative to a critical value $\Psi_{\rm crit} \sim 1$ which separates quiescent burning from large-scale detonations. The exact value of this critical parameter is sensitive to details about the disk, such as the thermal content or the amplitude of the viscous stress (Table 3).

2. – For disks that include cooling and/or have $\Psi \gtrsim \Psi_{\rm crit}$, a detonation can be triggered by hot spots formed near the burning front (Fig. 3). These temperature enhancements are generated by turbulent mixing of cold fuel and hot ash (Fig. 4), which produce an induction time-gradient consistent with that required to generate a detonation via the Zel'dovich mechanism (Fig. 4; Appendix C). For low values of Ψ, detonations remain localized, and provide at most a slight enhancement to the mass ejection in quiescent disks.

Increasing Ψ gives rise to detonations of increasing power.

3. – Exploding disks ($\Psi \gg \Psi_{\rm crit}$) can easily achieve expansion velocities in excess of $1,000$ km s^{-1} (Table 3). A remnant disk, with a mass typically a few percent of the initial WD mass, is left behind (Fig. 6).

4. – Non-exploding disks with nuclear reactions can generate unbound outflows along a funnel next to the rotation axis (Fig. 9). This material is composed primarily of nuclear ash. The expansion velocity of these outflows can also achieve ~ 1000 km s^{-1} (Fig. 10), with mass outflow rates spanning the range $10^{-5} - 10^{-3}$ $M_\odot$ s^{-1} (Table 3).

5. – The energy deposition by nuclear reactions locally enhances the turbulent kinetic energy, decreasing the mass accretion rate with increasing Ψ (Fig. 8). Given that a significant fraction of the outflowing material is bound and hence returns to the disk (Fig. 9), this choking of accretion can prolong the lifetime of the disk well beyond a few viscous times. A significant amount of burnt material can then accumulate at large distances from the disk.

6. – Outflows from the disk, generated either via quiescient disk winds or a large-scale detonation, may give rise to an optical supernova powered by the radioactive decay of ^{56}Ni. In the case of a disk detonation, some of the properties of the predicted transient are consistent with those of the observed class of unusual Type Ia SNe defined by SN 2002cx.

This study has focused primarily on characterizing the range of outcomes obtained in different regions of parameter space, and on identifying the main parameter dependencies. Given the number of approximations made, our results cannot be directly translated into observational predictions, nor do they constitute definitive statements about the likely outcome of a realistic WD/NS or WD/BH merger. Aside from including a realistic equation of state and a full nuclear reaction network, a convergence study on the circum-torus medium needs to be performed in order to reliably predict expansion velocities and thermodynamic properties of the ejecta. Also, fully three-dimensional simulations are eventually desirable, since the formation and ignition of hot spots is likely to occur at a position which is well-localized in azimuth, an effect clearly not captured by an axisymmetric calculation.

Even if NuDAFs in nature turn out not to explode, the fact that realistic burning rates yield $\Psi > 1$ (Table 2) implies that the structure and evolution of these disks will indeed be rich due to the multiple elements to be burned and the dynamical importance of each of these reactions. For example, despite the fact that model CO_f1 [full ^{12}C(^{12}C,γ)^{24}Mg rate] does not achieve explosion, the mass loss rate in the unbound material is ~ 100 times the net accretion rate at the inner boundary. A significant fraction of the disk will be ejected as an unbound flow at high velocities over a timescale $\sim 100 t_{\rm orb} \sim$ few hr. The observational signature of such an event may constitute a unique type of transient, which is distinct from that produced in the case of disk detonation or as yet observed.

A companion paper will continue the study of these disks using a realistic equation of state and a full nuclear reaction network.

APPENDIX

A. UNIT CONVERSION AND BURNING RATES

For completeness, this Appendix show explicitly the conversion from physical to code units and the functional forms of the reactions used.

The code takes the circularization radius R_0, the orbital velocity at this radius $(GM_c/R_0)^{1/2}$, and the maximum initial torus density

$$\rho_{\text{uni}} = 1.5 \times 10^5 \left(\frac{\rho_{\text{max}}}{\bar{\rho}}\right) \left(\frac{M_{\text{WD}}}{0.6M_\odot}\right) \left(\frac{10^{9.3}\,\text{cm}}{R_0}\right)^3 \text{g cm}^{-3}, \tag{A1}$$

as the basic set of units. In equation (A1), $(\rho_{\text{max}}/\bar{\rho})$ is the ratio of the maximum to average density in the torus. This quantity is obtained by computing the total torus mass using the density profile in equation (26), being a function of the adiabatic index and distortion parameter only. For $\gamma = 5/3$ and $d = \{1.2, 1.5, 3\}$, the result is $\rho_{\text{max}}/\bar{\rho} = \{0.536, 0.176, 2.47 \times 10^{-2}\}$. The temperature corresponding to $p/\rho = GM_c/R_0$ is

$$T_{\text{uni}} = 2 \times 10^9 \left(\frac{\mu}{1.75}\right) \left(\frac{M_c}{1.4M_\odot}\right) \left(\frac{10^{9.3}\,\text{cm}}{R_0}\right) \text{K}, \tag{A2}$$

where μ is given by equation (7). The mean molecular weight for temperature conversion purposes is calculated using the initial composition of the disk, once per model. Given the pressure and density in code units, we use equations (A1) and (A2) to obtain physical density and temperature

The specific energy generation rates in physical units are converted to code units through division by

$$\frac{1}{R_0}\left(\frac{GM_c}{R_0}\right)^{3/2} \simeq 1.4 \times 10^{16} \left(\frac{M_c}{1.4M_\odot}\right)^{3/2}$$
$$\times \left(\frac{10^{9.3}\,\text{cm}}{R_0}\right)^{5/2} \text{erg g}^{-1}\,\text{s}^{-1} \tag{A3}$$

The rate of change of mass fractions is converted to code units through multiplication by

$$\left(\frac{R_0^3}{GM_c}\right)^{1/2} \simeq 6.5 \left(\frac{R_0}{10^{9.3}\,\text{cm}}\right)^{3/2} \left(\frac{1.4M_\odot}{M_c}\right)^{1/2} \text{s}. \tag{A4}$$

Analytic nuclear burning rates are taken from Caughlan & Fowler (1988)[12]. The bulk of our study makes use of the $^{12}\text{C}(^{12}\text{C},\gamma)^{24}\text{Mg}$ reaction, which is the most energetic among the α reactions involving carbon, oxygen, and helium. The specific energy generation rate is

$$\dot{Q}_{\text{nuc, c12}} = 3.96 \times 10^{43} \rho_1 X_C^2 \frac{T_{A9}^{5/6}}{T_9^{3/2}} \times$$
$$\exp\left(-\frac{84.165}{T_{A9}^{1/3}} - 2.12 \times 10^{-3} T_9^3\right) \text{erg g}^{-1}\,\text{s}^{-1}, \tag{A5}$$

where ρ_1 is the density in g cm^{-3}, $T_9 = T/(10^9\,\text{K})$, X_C is the mass fraction of ^{12}C, and

$$T_{A9} = \frac{T_9}{1 + 0.0396 T_9}. \tag{A6}$$

The rate of change of X_C is given by

$$\dot{X}_{C,c12} = -\frac{m_C}{Q_{12}} \dot{Q}_{\text{nuc, 12}}, \tag{A7}$$

where $m_C = 12 m_n$ is the mass of a carbon nucleus, and $Q_{12} = 13.933$ MeV is the energy liberated in the reaction.

---

[12] http://www.phy.ornl.gov/astrophysics/data/cf88/

To gain an analytic understanding of the effect of nuclear burning, we also use an approximate power-law form of the ^{12}C(^{12}C,γ)^{24}Mg reaction. Following a standard procedure (e.g., Kippenhahn & Weigert 1994), we expand equation (A5) in a Taylor series in temperature around the point where nuclear burning is equal to the dynamical time, and obtain

$$\dot{Q}_{\mathrm{nuc,pl}} = 3.06 \times 10^6 X_{\mathrm{C}}^2 \rho_1 T_9^{29}\,\mathrm{erg\ g^{-1}\ s^{-1}}. \tag{A8}$$

The change in the carbon mass fraction is obtained from equation (A7) by replacing the energy generation rate. Good agreement between the two formulations is found in the temperature range $[0.6, 1.2] \times 10^9$ K. At higher temperatures, the full rate has an increasingly weaker dependence on temperature relative to the power-law approximation.

To consider the case of helium white dwarfs, we also include the triple-alpha reaction. The energy generation rate is

$$\dot{Q}_{\mathrm{nuc,3\alpha}} = 5.07 \times 10^8 X_{\mathrm{He}}^3 \rho_1^3 T_9^{-3} \exp\left(-\frac{4.4027}{T_9}\right)$$
$$+ 2.45 \times 10^9 r_{28} X_{\mathrm{He}}^3 \rho_1^3 T_9^{-3/2} \exp\left(-\frac{24.811}{T_9}\right), \tag{A9}$$

where X_{He} is the mass fraction in helium nuclei. The coefficient r_{28} is set to $1/10$. The rate of change of the helium mass fraction is

$$\dot{X}_{\mathrm{He}} = -\frac{Q_{3\alpha}}{m_{\mathrm{C}}}\dot{Q}_{\mathrm{nuc,3\alpha}}, \tag{A10}$$

where $Q_{3\alpha} = 7.275$ MeV is the energy released in the reaction.

B. VERIFICATION TESTS

This Appendix describes a series of tests conducted on the implementation of the NuDAF setup in FLASH3.2 (§3.3).

We first tested the degree to which the torus can remain in steady-state in the absence of viscous source terms. To this end, we use a torus with $d = 1.125$, and an isothermal atmosphere with $\rho_{\mathrm{at}} = 10^{-6}\rho_{\mathrm{max}}$ at $r_{\mathrm{at}} = 0.4R_0$ (eq. [28]). The computational domain extends from $r_{\mathrm{in}} = 0.4R_0$ to $r_{\mathrm{out}} = 4R_0$, and the resolution is $N_r = 64$, with 90 uniformly spaced cells covering the full range of polar angles. Numerical diffusion causes a very small amount of mass to peel off from the torus edges and accrete through the inner boundary. At our baseline resolution (§3.3), the total angular momentum in the computational domain is conserved to within a few parts in 10^{-6} over 10 orbits. The mass and angular momentum inside torii (defined as the material inside an iso-density surface at $10^{-3}\rho_{\mathrm{max}}$), are conserved to within a few parts in 10^{-4} over 10 orbits. Over the same time interval, the maximum torus density decreases by slightly more than 1%.

The inner boundary condition (eq. [33]) was tested by evolving a torus similar to that used in the previous test, but now with neither angular momentum nor viscosity. Under such conditions, the system proceeds to free-fall towards the gravitating mass. For an inner boundary with diameter comparable to the torus thickness ($r_{\mathrm{in}} = 0.4R_0$), the torus material is cleanly absorbed by the inner radial boundary, with no transients being generated. Using a smaller inner radius ($r_{\mathrm{in}} = 0.04R_0$) causes some material to collide with the symmetry axis, but the bulk of the torus is still cleanly accreted, with no discernible feedback from the boundary.

To test the accuracy of our viscous diffusion operator, we multiply equation (22) by ℓ_z, make use of equations (20) and (29), and integrate over volume, to obtain

$$\frac{\partial}{\partial t}L_2 + \int \mathrm{d}^3 x\,\mathbf{F}_\ell \cdot \nabla \ell_z = 0, \tag{B1}$$

where

$$L_2 = \int \mathrm{d}^3 x \left(\frac{1}{2}\rho\ell_z^2\right), \tag{B2}$$

and the integral is carried out over the full computational domain. For equation (B1) to be satisfied, the advection of ℓ_z and the flux formulation of the viscous operator must be treated correctly (T. Heinemann, private communication). Figure 12 shows the relative difference between the two terms in equation (B1), averaged over the first orbit, for a test model evolved with different spatial resolutions. The torus has $d = 1.125$ and a viscosity proportional to density (eq. [15]), with $\tilde{\nu}_0 = 0.01$. Values lie between 10^{-3} and 10^{-2} depending on resolution. A number of operations are involved in computing this equation, which degrade its accuracy, thus we consider the results as indicative of our correct treatment of viscous diffusion within the limitations of the hydrodynamic method.

As an additional test of angular momentum transport, we compared the result of using the flux-conservative formulation for angular momentum transport (eqns. [29] and [30]) with the result of directly computing the divergence of the viscous stress tensor

$$(\nabla \cdot \mathbb{T})_\phi = \frac{1}{r^3}\frac{\partial}{\partial r}\left(r^3 T_{\mathrm{r}\phi}\right) + \frac{1}{\sin^2\theta}\frac{\partial}{\partial\theta}\left(\sin^2\theta\,T_{\theta\phi}\right) \tag{B3}$$

as a 3-point finite difference operator. The result differs at the edges and surroundings of the torus, with the flux formulation maintaining a sharper torus surface (in ℓ_z) for a longer time. Inside the torus, the evolution is nearly identical within stochastic fluctuations induced by convection.
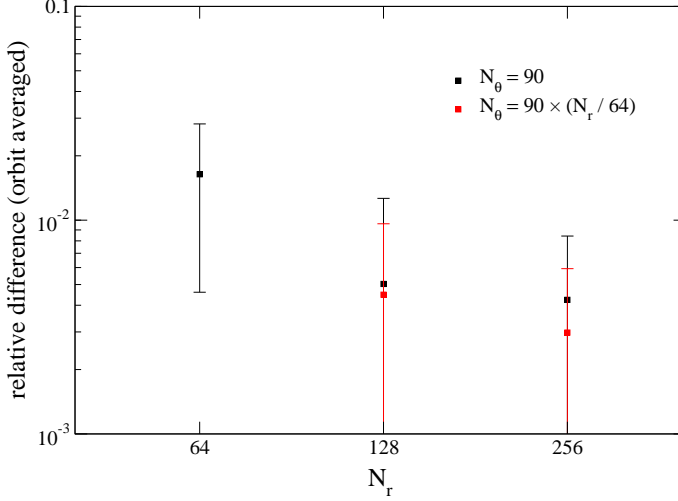
FIG. 12.— Relative difference between the two terms appearing in equation (B1), normalized relative to the second term, and averaged between 20% and 80% of the first orbit. The torus has $d = 1.125$, inner and outer radii $r_{in} = 0.4R_0$ and $r_{out} = 4R_0$, respectively, and a viscosity given by equation (15) with $\bar{\nu}_0 = 0.01$. The quantities N_r and N_θ denote the number of grid cells per decade in radius and in the polar direction, respectively. The error bars denote the root-mean-square fluctuation of the difference, which is due to fluctuations in the time derivative of equation (B2), computed as a time-centered finite difference with time step equal to $1/1000$ of an orbital period.

C. CONDITIONS FOR DETONATION VIA TURBULENT MIXING

In this Appendix we evaluate whether the turbulent mixing of ash and fuel can generate the conditions for a detonation in NuDAFs. The Zel'dovich criterion for spontaneous initiation of a detonation is that disparate portions of the burning region be separated by a distance such that the difference in the timescale for nuclear heating implies a supersonic phase velocity (Zel'dovich et al. 1970; Blinnikov & Khokhlov 1987; Woosley 1990). Quantitatively, this condition is expressed as (e.g., Niemeyer & Woosley 1997; Bell et al. 2004)

$$|\nabla t_{ind}|^{-1} > c_s, \tag{C1}$$

where c_s is the adiabatic sound speed and t_{ind} is the induction time, which is loosely defined as the time required to 'run away' to high temperatures via burning at constant pressure. Since $t_{ind} \propto c_s^2/\dot{Q}_{nuc}$ is a rapidly decreasing function of temperature, a shallow temperature gradient is required across the burning region for triggering a detonation. Such a condition may be satisfied in NuDAFs due to the effects of turbulent mixing.

We focus on the burning of fuel with an initial mass fraction X_{f0}. The steady-state structure of the accretion flow is characterized by two radially-separated regions: (1) unburned fuel with temperature T_f and density ρ_f; and (2) burned ash with temperature T_a and density ρ_a. The burning front separating the upstream (region 1) from the downstream (region 2) is centered about the radius $r \equiv r_{nuc}$ (eq. [39]) and has a width Δr_{nuc}. The radius r_{nuc} is approximately determined by equality of the fuel consumption time $t_{nuc} = X_f/\dot{X}_f$ and the dynamical timescale $t_{dyn} = (r^3/GM)^{1/2}$.

If burning occurs at constant pressure, then conservation of mass and enthalpy determines the change in density and temperature across the burning front (e.g., Khokhlov et al. 1997):

$$\frac{\rho_a}{\rho_f} = \frac{T_f}{T_a} = \frac{1}{1+\Psi} \quad (P_{gas} \gg P_{rad}), \tag{C2}$$

$$\frac{\rho_a}{\rho_f} = \frac{1}{1+\Psi}; \quad T_f = T_a \quad (P_{rad} \gg P_{gas}), \tag{C3}$$

where

$$\Psi = (\gamma-1)\frac{\varepsilon_{nuc}}{c_{s,f}^2} \tag{C4}$$

is the ratio of the specific nuclear energy released per reaction (eq. [19]) to the enthalpy of the fuel $c_{s,f}^2/(\gamma-1)$ (see also equation [37]). We have separated cases corresponding to whether gas or radiation pressure dominates.

Due to the turbulent nature of accretion and RT instabilities, the burning front at $r = r_{nuc}$ is not completely smooth (e.g., Fig. 3). Instead, parcels of burned ash occasionally mix with the colder fuel upstream. If mixing produces conditions such that equation (C1) is satisfied over the length of the eddy L_{edd}, then a detonation may be triggered. If a fraction f_a of ash is mixed with a fraction $1-f_a$ of fuel (resulting in a reactant mass fraction $X_m = [1-f_a]X_{f0}$), then the density ρ_m and temperature T_m of the resulting mixture are also determined by conservation of mass and enthalpy:

$$\frac{\rho_m}{\rho_f} = \frac{T_f}{T_m} = \frac{1}{1+f_a\Psi} \quad (P_{gas} \gg P_{rad}), \tag{C5}$$

$$\frac{\rho_m}{\rho_f} = \frac{1}{1+f_a\Psi}; \quad T_m = T_f \quad (P_{rad} \gg P_{gas}), \tag{C6}$$

The length of an eddy $L_{\rm edd}$ which is capable of efficient mixing must obey $\Delta r_{\rm nuc} \lesssim L_{\rm edd} \lesssim H = r_{\rm nuc}/2$ since it must both fit inside the disk midplane and it must sample both fuel and ash over the width of the mixing region $\Delta r_{\rm nuc}$. The condition for detonation in equation (C1) can thus approximately be written as

$$|\nabla t_{\rm ind}|^{-1} \sim \frac{L_{\rm edd}}{t_{\rm ind}(X_{\rm m}, \rho_{\rm m}, T_{\rm m})} > c_s \tag{C7}$$

or

$$\left(\frac{L_{\rm edd}}{H}\right) > \frac{t_{\rm ind}(X_{\rm m}, \rho_{\rm m}, T_{\rm m})}{t_{\rm orb}(r_{\rm nuc})}, \tag{C8}$$

where we have assumed that the sound speed of the mixture is similar to that in the disk midplane, and we have used the condition of vertical hydrostatic equilibrium $c_s = H/t_{\rm orb}$.

Assuming a burning rate of the general form $\dot{Q}_{\rm nuc} \propto \varepsilon_{\rm nuc} X^q \rho^{q-1} T^\beta$ (eq. [A8]), one has that $t_{\rm ind} \propto \rho^{-(q-1)} X^{-q} T^{-\beta}/[\Psi \bar{\beta}]$ for burning at constant pressure, where the factor of $\bar{\beta}$ in the denominator accounts for the fact that runaway to high temperatures occurs on a timescale which is shorter than the heating timescale estimated using the initial heating rate when gas pressure dominates ($\bar{\beta} \simeq \beta$ when $P_{\rm gas} \gg P_{\rm rad}$; $\bar{\beta} \simeq 1$ when $P_{\rm rad} \gg P_{\rm gas}$). Since $t_{\rm nuc} = X/\dot{X} \propto \rho^{-(q-1)} X^{-(q-1)} T^{-\beta}$, we also have $t_{\rm nuc} \simeq \Psi \bar{\beta} t_{\rm ind}$. Using the relation $t_{\rm nuc}(X_{\rm f}, \rho_{\rm f}, T_{\rm f}) = t_{\rm dyn}$ that determines $r_{\rm nuc}$, one can rewrite equation (C8) as

$$\frac{L_{\rm edd}}{H} > \frac{1}{2\pi\bar{\beta}\Psi}\left[\frac{t_{\rm ind}(X_{\rm m}, \rho_{\rm m}, T_{\rm m})}{t_{\rm ind}(X_{\rm f}, \rho_{\rm f}, T_{\rm f})}\right], \tag{C9}$$

or

$$\frac{L_{\rm edd}}{H} > \frac{1}{2\pi\bar{\beta}\Psi}\left(\frac{c_{\rm s,m}^2}{c_{\rm s,f}^2}\right)\left(\frac{\rho_{\rm f}}{\rho_{\rm m}}\right)^{q-1}\left(\frac{X_{\rm f}}{X_{\rm m}}\right)^q\left(\frac{T_{\rm f}}{T_{\rm m}}\right)^\beta$$
$$> \frac{1}{2\pi\Psi}\left(\frac{1}{1-f_{\rm a}}\right)^q \begin{cases} \beta^{-1}(1+f_{\rm a}\Psi)^{q-\beta}, & (P_{\rm gas}/P_{\rm rad}) \gg 1 \\ (1+f_{\rm a}\Psi)^q, & (P_{\rm rad}/P_{\rm gas}) \gg 1 \end{cases}, \tag{C10}$$

where we have used the results from equation (C6).

Equation (C10) shows that in a gas pressure-dominated flow, even small eddies with $L_{\rm edd} \sim 0.1H$, such as those producing detonations in our simulations (Fig. 3), require only a moderate amount of entrained fuel $f_a \ll 1$ to satisfy the condition for a detonation given a temperature-sensitive reaction (e.g., $\beta = 29$, $q = 2$; eq. [A8]). The mixed fraction of upstream ash is indeed small ($X_a \sim$ few %) in the regions which form hot spots and detonations in our simulations (see Fig. 4). The sensitive dependence of the bracketed quantity on the RHS on Ψ (almost exponential) may in part also explain why the formation of a detonation in our simulations depends sensitively on this value. On the other hand, in a radiation pressure dominated disk the condition (C10) is more challenging to satisfy, as the lack of temperature fluctuations cause mixing to be detrimental given the decrease in density (eq. [C6]).

Producing a detonation is harder than satisfying condition (C10), since mixing must occur before complete burning. Another important parameter is thus the ratio of the characteristic eddy turnover timescale $t_{\rm edd} \sim L_{\rm edd}/v_{\rm edd} = \mathcal{M}^{-1}L_{\rm edd}/c_s$, which sets the timescale for mixing, to the burning timescale of the mixture $t_{\rm nuc}$:

$$\frac{t_{\rm nuc}}{t_{\rm edd}} = \mathcal{M}\Psi\bar{\beta}\left(\frac{c_s}{L_{\rm edd}/t_{\rm ind}}\right), \tag{C11}$$

where $\mathcal{M} \equiv v_{\rm edd}/c_s < 1$ is the turbulent Mach number. Provided that the condition for detonation (eq. [C8]) is marginally achieved, equation (C11) shows that efficient mixing requires a combination of vigorous turbulence and/or strong energy release. Dominance of radiation pressure makes mixing more inefficient, which is helpful in satisfying equation (C10), as a higher mixing fraction results in a larger required eddy size.

REFERENCES

Abramowicz, M. A., Lasota, J.-P., & Igumenshchev, I. V. 2000, MNRAS, 314, 775
Arnett, W. D., & Meakin, C. 2011, ApJ, 733, 78
Bailyn, C. D., Jain, R. K., Coppi, P., & Orosz, J. A. 1998, ApJ, 499, 367
Balbus, S. A., & Hawley, J. F. 1998, Reviews of Modern Physics, 70, 1
Belczynski, K., Bulik, T., & Rudak, B. 2002, ApJ, 571, 394
Bell, J. B., Day, M. S., Rendleman, C. A., Woosley, S. E., & Zingale, M. 2004, ApJ, 608, 883
Beloborodov, A. M., Stern, B. E., & Svensson, R. 2000, ApJ, 535, 158
Blandford, R. D., & Begelman, M. C. 1999, MNRAS, 303, L1
Blandford, R. D., & Payne, D. G. 1982, MNRAS, 199, 883
Blinnikov, S. I., & Khokhlov, A. M. 1987, Soviet Astronomy Letters, 13, 364
Blinnikov, S. I., Röpke, F. K., Sorokina, E. I., Gieseler, M., Reinecke, M., Travaglio, C., Hillebrandt, W., & Stritzinger, M. 2006, A&A, 453, 229
Bodenheimer, P., & Woosley, S. E. 1983, ApJ, 269, 281

Caughlan, G. R., & Fowler, W. A. 1988, Atomic Data and Nuclear Data Tables, 40, 283
Chen, W.-X., & Beloborodov, A. M. 2007, ApJ, 657, 383
Chevalier, R. A. 1993, ApJ, 411, L33
Chornock, R., Filippenko, A. V., Branch, D., Foley, R. J., Jha, S., & Li, W. 2006, PASP, 118, 722
Colella, P., & Woodward, P. R. 1984, JCP, 54, 174
Davis, S. W., Stone, J. M., & Pessah, M. E. 2010, ApJ, 713, 52
Di Matteo, T., Perna, R., & Narayan, R. 2002, ApJ, 579, 706
Dubey, A., Antypas, K., Ganapathy, M. K., Reid, L. B., Riley, K., Sheeler, D., Siegel, A., & Weide, K. 2009, J. Par. Comp., 35, 512
Eggleton, P. P. 1983, ApJ, 268, 368
Fernández, R. 2012, ApJ, 749, 142
Foley, R. J., Chornock, R., Filippenko, A. V., Ganeshalingam, M., Kirshner, R. P., Li, W., Cenko, S. B., Challis, P. J., Friedman, A. S., Modjaz, M., Silverman, J. M., & Wood-Vasey, W. M. 2009, AJ, 138, 376

Foley, R. J., Rest, A., Stritzinger, M., Pignata, G., Anderson, J. P., Hamuy, M., Morrell, N. I., Phillips, M. M., & Salgado, F. 2010, AJ, 140, 1321
Fryer, C. L., Belczynski, K., Wiktorowicz, G., Dominik, M., Kalogera, V., & Holz, D. E. 2012, ApJ, 749, 91
Fryer, C. L., & Woosley, S. E. 1998, ApJ, 502, L9
Fryer, C. L., Woosley, S. E., Herant, M., & Davies, M. B. 1999, ApJ, 520, 650
Hawley, J. F., & Balbus, S. A. 2002, ApJ, 573, 738
Hawley, J. F., Balbus, S. A., & Stone, J. M. 2001, ApJ, 554, L49
Hawley, J. F., Gammie, C. F., & Balbus, S. A. 1995, ApJ, 440, 742
Hirose, S., Krolik, J. H., & Stone, J. M. 2006, ApJ, 640, 901
Igumenshchev, I. V., & Abramowicz, M. A. 1999, MNRAS, 303, 309
Igumenshchev, I. V., & Abramowicz, M. A. 2000, ApJS, 130, 463
Igumenshchev, I. V., Abramowicz, M. A., & Narayan, R. 2000, ApJ, 537, L27
Igumenshchev, I. V., Narayan, R., & Abramowicz, M. A. 2003, ApJ, 592, 1042
Itoh, N., Hayashi, H., Nishikawa, A., & Kohyama, Y. 1996, ApJS, 102, 411
Jha, S., Branch, D., Chornock, R., Foley, R. J., Li, W., Swift, B. J., Casebeer, D., & Filippenko, A. V. 2006, AJ, 132, 189
Kasliwal, M. M., et al. 2011, arXiv:1111.6109
Khokhlov, A. M., Oran, E. S., & Wheeler, J. C. 1997, ApJ, 478, 678
King, A., Olsson, E., & Davies, M. B. 2007, MNRAS, 374, L34
Kippenhahn, R., & Weigert, A. 1994, Stellar Structure and Evolution, 2nd edn. (New York: Springer)
Landau, L. D., & Lifshitz, E. M. 1987, Fluid Mechanics, 2nd edn. (Oxford: Butterworth-Heinemann)
Larson, R. B. 1984, MNRAS, 206, 197
Li, W., et al. 2003, PASP, 115, 453
Lindner, C. C., Milosavljević, M., Couch, S. M., & Kumar, P. 2010, ApJ, 713, 800
Lindner, C. C., Milosavljević, M., Shen, R., & Kumar, P. 2012, ApJ, 750, 163
Lisewski, A. M., Hillebrandt, W., Woosley, S. E., Niemeyer, J. C., & Kerstein, A. R. 2000, ApJ, 537, 405
MacFadyen, A. I., & Woosley, S. E. 1999, ApJ, 524, 262
Machida, M., Matsumoto, R., & Mineshige, S. 2001, PASJ, 53, L1
McKinney, J. C., Tchekhovskoy, A., & Blandford, R. D. 2012, MNRAS, 423, 3083
Metzger, B. D. 2012, MNRAS, 419, 827
Metzger, B. D., Thompson, T. A., & Quataert, E. 2008, ApJ, 676, 1130
Milosavljević, M., Lindner, C. C., Shen, R., & Kumar, P. 2012, ApJ, 744, 103
Narayan, R., Sadowski, A., Penna, R. F., & Kulkarni, A. K. 2012, MNRAS, submitted, arXiv:1206.1213
Narayan, R., & Yi, I. 1994, ApJ, 428, L13
—. 1995, ApJ, 444, 231
Nauenberg, M. 1972, ApJ, 175, 417
Niemeyer, J. C., & Woosley, S. E. 1997, ApJ, 475, 740
Nomoto, K., & Kondo, Y. 1991, ApJ, 367, L19
O'Shaughnessy, R., & Kim, C. 2010, ApJ, 715, 230
Pang, B., Pen, U.-L., Matzner, C. D., Green, S. R., & Liebendörfer, M. 2011, MNRAS, 415, 1228
Papaloizou, J. C. B., & Pringle, J. E. 1984, MNRAS, 208, 721
Paschalidis, V., Liu, Y. T., Etienne, Z., & Shapiro, S. L. 2011, Phys. Rev. D, 84, 104032
Paschalidis, V., MacLeod, M., Baumgarte, T. W., & Shapiro, S. L. 2009, Phys. Rev. D, 80, 024006
Pen, U.-L., Matzner, C. D., & Wong, S. 2003, ApJ, 596, L207
Perets, H. B., et al. 2010, Nature, 465, 322
Phillips, M. M., et al. 2007, PASP, 119, 360
Plewa, T., & Müller, E. 1999, A&A, 342, 179
Quataert, E., & Gruzinov, A. 2000, ApJ, 539, 809
Quataert, E., & Shiode, J. 2012, MNRAS, 423, L92
Schwab, J., Shen, K. J., Quataert, E., Dan, M., & Rosswog, S. 2012, MNRAS, submitted, arXiv:1207.0512
Shakura, N. I., & Sunyaev, R. A. 1973, A&A, 24, 337
Shi, J., Krolik, J. H., & Hirose, S. 2010, ApJ, 708, 1716
Siess, L., & Livio, M. 1999, MNRAS, 304, 925
Sim, S. A., Röpke, F. K., Hillebrandt, W., Kromer, M., Pakmor, R., Fink, M., Ruiter, A. J., & Seitenzahl, I. R. 2010, ApJ, 714, L52
Stone, J. M., & Norman, M. L. 1992, ApJS, 80, 753
Stone, J. M., & Pringle, J. E. 2001, MNRAS, 322, 461
Stone, J. M., Pringle, J. E., & Begelman, M. C. 1999, MNRAS, 310, 1002
Surman, R., McLaughlin, G. C., & Sabbatino, N. 2011, ApJ, 743, 155
Thöne, C. C., et al. 2011, Nature, 480, 72
Waldman, R., Sauer, D., Livne, E., Perets, H., Glasner, A., Mazzali, P., Truran, J. W., & Gal-Yam, A. 2011, ApJ, 738, 21
Wickramasinghe, D. T., & Ferrario, L. 2000, PASP, 112, 873
Woosley, S. E. 1990, in Supernovae, ed. A. G. Petschek, 182–212
Woosley, S. E., Blinnikov, S., & Heger, A. 2007, Nature, 450, 390
Woosley, S. E., & Heger, A. 2006, ApJ, 637, 914
Woosley, S. E., Heger, A., & Weaver, T. A. 2002, Reviews of Modern Physics, 74, 1015
Yuan, F., Wu, M., & Bu, D. 2012, ApJ, submitted, arXiv:1206.4157
Zel'dovich, Y. B., Librovich, V. B., Makhviladze, G. M., & Sivashinskil, G. I. 1970, J. Appl. Mech. & Tech. Phys., 11, 264